

# *Projected near-term changes in three types of heat waves over China under RCP4.5*

Article

Accepted Version

Su, Q. and Dong, B. (2019) Projected near-term changes in three types of heat waves over China under RCP4.5. *Climate Dynamics*, 53 (7-8). pp. 3751-3769. ISSN 0930-7575 doi: <https://doi.org/10.1007/s00382-019-04743-y> Available at <http://centaur.reading.ac.uk/83090/>

It is advisable to refer to the publisher's version if you intend to cite from the work. See [Guidance on citing](#).

Published version at: <https://link.springer.com/article/10.1007/s00382-019-04743-y>

To link to this article DOI: <http://dx.doi.org/10.1007/s00382-019-04743-y>

Publisher: Springer

All outputs in CentAUR are protected by Intellectual Property Rights law, including copyright law. Copyright and IPR is retained by the creators or other copyright holders. Terms and conditions for use of this material are defined in the [End User Agreement](#).

[www.reading.ac.uk/centaur](http://www.reading.ac.uk/centaur)

## **CentAUR**

Central Archive at the University of Reading

Reading's research outputs online

1 **Projected near-term changes in three types of heat waves over China**  
2 **under RCP4.5**

3 Su Qin<sup>1</sup> and Buwen Dong<sup>2</sup>

4  
5 <sup>1</sup> Department of Atmospheric Sciences, Yunnan University, Kunming, China

6 <sup>2</sup> National Centre for Atmospheric Science-Climates, Department of Meteorology,  
7 University of Reading, Reading, UK

8

9

10

11

12

13

14

15

16

17

18

19

20

21 Corresponding author:

22 Qin Su,

23 Department of Atmospheric Sciences,

24 Yunnan University,

25 Kunming, 650091, China

26 E-mail: suqin@ynu.edu.cn

27

28 **Abstract**

29       The future changes in three aspects of frequency, intensity, and duration of the  
30 compound, daytime, and nighttime heat waves (HWs) over China during extended  
31 summer (May–September) in a future period of the mid-21<sup>st</sup> century (FP; 2045-2055)  
32 under RCP4.5 scenario relative to present day (PD; 1994-2011) are investigated by two  
33 models, i.e. MetUM-GOML1 and MetUM-GOML2, comprising the atmospheric  
34 components of two state-of-the-art climate models coupled to a multi-level mixed-layer  
35 ocean model. The results show that all three types of HWs over China will occur more  
36 frequently with strengthened intensity and elongated duration in the mid-21<sup>st</sup> century.  
37 The compound HWs will change most dramatically with the frequency in the FP being  
38 4-5 times that in the PD, and the intensity and duration doubling those in the PD. The  
39 changes of daytime and nighttime HWs are also remarkable, with the changes of  
40 nighttime HWs larger than those of daytime HWs. The future changes of the three types  
41 of HWs over China in two models are similar in terms of spatial patterns and area  
42 averaged quantities, indicating these projected changes of HWs over the China under  
43 RCP4.5 scenario are robust. The further analyses suggest that projected future changes  
44 of HWs over China are predominantly determined by the increase in seasonal mean  
45 surface air temperatures with change in temperature variability playing a minor role.  
46 The seasonal mean temperature increases are partly due to the increase in surface  
47 downward longwave radiation and partly due to the increase in surface shortwave  
48 radiation. The increased downward longwave radiation results from the enhanced  
49 greenhouse effect and the increased water vapor in the atmosphere. The increased

50 surface shortwave radiation results from the decreased aerosol emissions via direct  
51 aerosol-radiation interaction and indirect aerosol-cloud interaction over southeastern  
52 and northeastern China and the decreased cloud cover related to reduced relative  
53 humidity.

54 **Key words:** heat waves, heat wave types, future changes, China, coupled models.

## 55 **1. Introduction**

56 Heat waves are usually defined as abnormally hot weather lasting for several days  
57 (Perkins and Alexander 2013; Perkins 2015). This distinct type of extreme temperature  
58 events has caused substantial damages to socioeconomics and human health (e.g.  
59 Robine et al. 2008; Coumou and Rahmstorf 2012; Hatfield and Prueger 2015; Lesk et  
60 al. 2016). In recent two decades, heat waves have occurred more frequently all over the  
61 world (e.g., Meehl and Tebaldi 2004; Seneviratne et al. 2014). Without any exception,  
62 several severe heat waves hit China recently in different regions and broke the regional  
63 historical temperature records, such as the 2013 July-August heat wave in the lower  
64 reaches of Yangtze River Valley (Sun et al. 2014; Zhou et al. 2014b; Ma et al. 2017),  
65 the 2015 summer heat wave in western China (Sun et al. 2016), and the 2017 July heat  
66 wave in central eastern China (Chen et al. 2018; Sparrow et al. 2018). These  
67 catastrophic events led to enormous economic loss and heat-related morbidity and  
68 mortality in China (e.g., Tan et al. 2007; Sun et al. 2016; Ma et al. 2017). The increased  
69 occurrence of heat waves largely results from the increased mean temperature (Argueso  
70 et al. 2016; Su and Dong 2019). As the increase in mean temperature will go on, how

71 the heat waves will change in the future under the global warming scenario is an  
72 important issue for developing climate adaptation strategies.

73 A heat wave could take place on daytime, nighttime, or both. With different timing  
74 of occurrence, the heat waves are related to different mechanisms and of different  
75 impacts (Gershunov et al. 2009, Freychet et al. 2017). The heat waves in the day, usually  
76 associated with dry conditions (Black et al. 2004; Gershunov et al. 2009; Wang et al.  
77 2016), have a variety of disastrous impacts on infrastructures, ecosystem, and human  
78 life (Wilbanks et al. 2012), while the heat waves at night, related to wet conditions  
79 (Gershunov et al. 2009; Chen and Lu 2014), have relatively weak impact. However,  
80 with the hot nights enhancing the damages of daytime high temperatures on human  
81 health (Gosling et al 2009), the heat waves persisting throughout the day and night are  
82 the most disastrous among these three types of heat waves (Karl and Knight 1997).  
83 Thus, recent studies applied a more precise classification of heat waves according to  
84 the timing of their occurrence to get more insights, which divided the heat waves into  
85 three types, i.e., daytime, nighttime and compound ones (e.g., Chen and Li 2017; Chen  
86 and Zhai 2017; Freychet et al. 2017; Su and Dong 2019).

87 In recent decades since the mid-20th century, the previously-defined heat waves,  
88 which only consider the daytime temperatures and involve the daytime heat waves and  
89 part of the compound heat waves, show increasing frequency and duration over China  
90 (Li et al. 2017; Luo and Lau 2017; Wang et al. 2017; You et al. 2017). Some recent  
91 studies, using the precisely defined daytime, nighttime, and compound heat waves over

92 most part of China, show significant increasing trends in frequency, intensity, and  
93 duration (Chen and Zhai 2017; Freychet et al. 2017). Particularly, the increase of  
94 frequency and intensity in compound and nighttime heat waves is much greater than  
95 that in daytime ones (Chen and Li 2017; Chen and Zhai 2017; Su and Dong 2019). The  
96 anthropogenic influences are highlighted to play crucial roles in the sharp increase in  
97 occurrence of the heat waves over China (e.g., Wilcox et al. 2015; Freychet et al. 2018).  
98 In more detail, Su and Dong (2019) reported that the increase in greenhouse gas  
99 concentration is responsible for the decadal increase in frequency, intensity, and spatial  
100 extent of the three types of heat waves over China across mid-1990s and the changes in  
101 anthropogenic aerosol emission lead to the increase in frequency and intensity of the  
102 daytime heat waves over Northeastern China and decrease the frequency and intensity  
103 of daytime HWs over Southeastern China.

104       Considering the anthropogenic influences, future changes in the heat waves and  
105 temperature extremes over China are assessed under different scenarios. There would  
106 be an increase in warm extremes and a decrease in cold extremes under a warming  
107 climate (Zhou et al. 2014a; Yu et al. 2018). The frequency and duration of previously-  
108 defined heat waves over China would increase and the increase would become larger  
109 when the mean temperature gets greater (Guo et al. 2017). However, only the future  
110 changes in previously-defined heat waves are estimated and the assessment of future  
111 changes in precisely defined compound, daytime, and nighttime heat waves is still  
112 lacking. Meanwhile all above projections have used fully coupled general circulation  
113 models (CGCMs). However, these CGCMs exhibit significant biases in simulated sea

114 surface temperature that challenge the reliability of climate projections (Wang et al.  
115 2014).

116 Therefore, the main aims of this work are to estimate the future changes of the  
117 daytime, nighttime, and compound heat waves over China and to reveal the associated  
118 physical processes by using two near-globally coupled models comprising the  
119 atmospheric components of two state-of-the-art climate models coupled to a multi-level  
120 mixed-layer ocean and having a much smaller bias in simulated sea surface temperature  
121 (Hirons et al. 2015, Dong et al. 2017, Luo et al. 2018). The structure of this paper is  
122 organized as follows: The model and experiments are described in Section 2. Model  
123 simulated extended seasonal mean surface air temperatures and definition of HWs are  
124 described in Section 3. The projected changes in the three types of heat waves are shown  
125 in Section 4. The physical processes responsible for future changes in heat waves are  
126 illustrated in Section 5. Conclusions are summarized in Section 6.

## 127 **2. Models and experiments**

### 128 **2.1 Models**

129 Two coupled models, MetUM-GOML1 and MetUM-GOML2 (Hirons et al. 2015),  
130 that comprise the atmospheric components of two state-of-the-art climate models  
131 coupled to a multi-level mixed-layer ocean model, are used in this study. The  
132 atmospheric component for MetUM-GOML1 is the Met Office Unified Model  
133 (MetUM) at the fixed scientific configuration Global Atmosphere 3.0 (GA3.0; Arribas  
134 et al. 2011; Walters et al. 2011). The atmospheric component for MetUM-GOML2 is



135 the MetUM GA6.0. The largest change in GA6.0 is that the “New Dynamics”  
136 dynamical core is replaced with “ENDGame” (Walters et al. 2014). ENDGame  
137 maintains the benefits of “New Dynamics”, whilst improving its accuracy, stability and  
138 scalability. The improved accuracy significantly reduces the model’s implicit damping,  
139 leading to a beneficial improvement to various modes of variability, such as the vertical  
140 height of extra-tropical cyclones and the structure of frontal systems. The details about  
141 GA6.0 are described in Walters et al. 2017. The resolution for these two atmospheric  
142 models is 1.875° longitude by 1.25° latitude with 85 vertical layers. The models include  
143 an interactive tropospheric aerosol scheme, which is able to simulate the direct, indirect  
144 and semi-direct effects of aerosols (Walters et al. 2011; Jones et al. 2011). The oceanic  
145 components for MetUM-GOML1 and MetUM-GOML2 are the same, which is a Multi-  
146 Column K Profile Parameterization (MC-KPP) mixed-layer ocean model. The  
147 horizontal resolution of MC-KPP is the same as the MetUM where it is coupled. The  
148 vertical resolution of MC-KPP is very high at the surface (1.2m) and near the surface  
149 (2 m over the first 41.5 m), since the MC-KPP columns with 100 levels over a depth of  
150 1000 m are defined using a stretch function. MC-KPP simulates only vertical mixing  
151 and does not include ocean dynamics, so the corrections for temperature and salinity  
152 based on the seasonally-varying 3-dimension temperature and salinity flux are  
153 prescribed to represent the mean ocean advection and account for biases in atmospheric  
154 surface heat and fresh water fluxes. The atmospheric and oceanic components are  
155 coupled every three hours. The air–sea coupling is limited by the maximum extent of a  
156 seasonally varying sea ice climatology (Hirons et al. 2015). These models are

157 computationally cheaper than models with a fully interactive ocean. More important,  
158 they have a smaller bias in simulated sea surface temperature (Hirons et al., 2015, Dong  
159 et al. 2017; Luo et al. 2018) in comparison with fully coupled models (e.g., Wang et al.  
160 2014) whilst also retaining intra-seasonal variability and coupling between the  
161 atmosphere and the ocean.

## 162 **2.2 Experiments**

163 The experiments performed in this study are summarized in Table 1. A 12-year  
164 relaxation experiment (R0) for both MetUM-GOML1 and MetUM-GOML2 models  
165 was firstly performed in which the MC-KPP profiles of temperature and salinity were  
166 relaxed to a present day (PD, 1994-2011) ocean temperature and salinity climatology  
167 derived from the Met Office ocean analysis (Smith and Murphy 2007). The relaxation  
168 experiment used PD anthropogenic greenhouse gas (GHG) and anthropogenic aerosol  
169 (AA) forcings (Lamarque et al. 2010; 2011). The daily mean seasonal cycle of ocean  
170 temperature and salinity corrections from the coupled relaxation experiment are then  
171 imposed in free-running coupled experiments. Three other time-sliced experiments  
172 using both models are performed by using different forcings, i.e. C-EP experiment  
173 forced by the early period (EP, 1964–1981) mean GHG concentrations and AA  
174 emissions, C-PD experiment forced by the PD (1994–2011) mean GHG concentrations  
175 and AA emissions, C-FP experiment forced by future period (FP, 2045-2055) mean  
176 GHG concentrations and AA emissions under the scenario of representative  
177 concentration pathway (RCP) 4.5. The single RCP4.5 scenario is chosen for

178 projection because the radiative forcings in the four scenarios of RCP2.6, RCP4.5,  
179 RCP6.0, and RCP8.5 do not differ significantly in the FP of the mid—21<sup>st</sup> century  
180 (Moss et al., 2010). Relative to PD means, FP mean GHG concentrations increase (CO<sub>2</sub>  
181 by 30%, CH<sub>4</sub> by 4.5%, and N<sub>2</sub>O by 10.4%) and the emission of sulfur dioxide, which  
182 is one of the most important aerosol species, decreases over the Europe (by 74%), the  
183 East Asia (by 79%), and the North America (by 81%) but increases over Indian sub-  
184 continent (Fig. 1). All experiments are run for 50 years and use the climatological PD  
185 sea ice extent from the Met Office Hadley Center Sea Ice and Sea Surface Temperature  
186 data set (HadISST; Rayner et al. 2003). The last 45 years of each experiment are used  
187 for analysis.

### 188 **3. Model simulated extended summer seasonal mean surface air temperatures** 189 **and HWs**

#### 190 **3.1 Model performance in simulating early period surface air temperatures**

191 The climatological means of daily maximum temperature (T<sub>max</sub>) and daily  
192 minimum temperature (T<sub>min</sub>) in the C-EP experiments of MetUM-GOML1 and  
193 MetUM-GOML2 for the extended summer are compared with the observed ones during  
194 EP (Fig. 2). The observational data used is the homogenized datasets of daily T<sub>max</sub> and  
195 T<sub>min</sub> series at 753 stations in China (Li et al. 2016). The observed T<sub>max</sub> pattern shows  
196 more or less uniform distributions over southeastern China with value higher than 28 °C  
197 and apparent meridional gradient over northeastern China. Over western China, a low  
198 value centre locates over the Tibetan Plateau and a high value centre is over

199 northwestern China with temperature above 28 °C (Fig. 2a). The observed  
200 climatological Tmin exhibits great meridional gradient over eastern China with the  
201 maximum higher than 22 °C in the southeast coast of China and minimum of 4-7 °C  
202 over northeastern China. The spatial distribution of Tmin over western China shows a  
203 minimum (less than 1 °C) over the Tibetan Plateau and a high value (more than 16 °C)  
204 over northwestern China, being similar to the spatial pattern in Tmax (Fig. 2b). The  
205 spatial patterns of climatological extended summer means of Tmax and Tmin and  
206 regional magnitudes in the C-EP experiments of MetUM-GOML1 and MetUM-  
207 GOML2 agree well with the observed ones with pattern correlation coefficients of 0.85  
208 and 0.86 for Tmax and 0.90 and 0.91 for Tmin (Fig. 2c-f). The two models reproduce  
209 the observed Tmax distributions over the southeastern and northwestern part of China  
210 with value above 28 °C, but slightly underestimate Tmax over the Tibetan Plateau and  
211 northeastern China (Fig. 2c and e). The observed Tmin distributions are also well  
212 simulated by the model, with some underestimation over the Tibetan Plateau (Fig. 2d).

### 213 **3.2 HWs definition**

214 Three types of HWs, namely compound, daytime, and nighttime HWs, are defined  
215 in this study in the same way as the former study on decadal changes across the mid-  
216 1990s over China (Su and Dong 2019). Considering the various climate types in China,  
217 the relative threshold, which is determined by local climate and varies at different places  
218 on different dates (Stefanon et al. 2012), is employed to define the heat waves over  
219 China in this study, as was used in some previous studies (e.g., Li et al. 2017; Chen and

220 Li 2017; Wang et al. 2017). The relative threshold on each model calendar day is  
221 calculated as the daily 90th percentile of daily Tmax or Tmin based on 15-day samples  
222 centered on that day during the last 45 years of C-EP experiment (i.e. total samples  
223  $15 \times 45 = 675$  days, Della-Marta et al. 2007). A compound HW, continuous hot weather  
224 in day and night, is defined when both Tmax and Tmin are higher than the thresholds  
225 for at least three days. A daytime (nighttime) HW, continuous hot weather only in the  
226 day (at night), is defined when only Tmax (Tmin) exceeds the thresholds for at least  
227 three days. All these three types of HWs are independent of each other.

228 Three indicators, i.e. frequency, intensity, and duration, are used to measure the  
229 HWs in a year. The frequency is represented by the accumulated occurrence of events  
230 within a year. The intensity of each event is calculated by averaging the everyday  
231 temperature exceedance above the threshold within an event. Particularly, the intensity  
232 of compound HWs is the sum of the averaged Tmax and Tmin exceedances. The  
233 duration of each event is the number of days when an event endures. The intensity and  
234 duration for a year is computed by averaging the intensity and duration of events  
235 occurring in that year.

### 236 **3.3 Model performance in simulating early period HWs**

237 The frequency, intensity, and duration of compound, daytime, and nighttime HWs  
238 in the C-EP experiment of MetUM-GOML1 and MetUM-GOML2 during the extended  
239 summer are compared with those in observations in the EP (Fig. S1-3). In observations,  
240 the frequency, intensity, and duration of compound HWs share similar spatial patterns,

241 with relatively large values over the southeastern China and the northern margin of  
242 mainland China (Fig. S1a-c). The daytime HWs in the EP are of the largest frequency  
243 and duration over the western China and of the greatest intensity over the northern  
244 margin of mainland China (Fig. S2a-c). The frequency and duration of nighttime HWs  
245 are relatively high over the central China and the intensity of nighttime HWs are the  
246 greatest over the northern margin of mainland China (Fig. S3a-c). The spatial patterns  
247 of the frequency, intensity, and duration of all three types of HWs in observations are  
248 well reproduced by these two models, despite the underestimation of the frequency and  
249 duration of daytime HWs over the western China. The biases of the area averaged  
250 indices are examined by using the relative bias, which is defined as the absolute bias  
251 (model simulated index minus observational one) divided by observational index. The  
252 relative biases for various regions range from -12% to -43% in MetUM-GOML1 and -  
253 2% to -55% in MetUM-GOML2. According to Guo et al. (2017), which used 12 CMIP5  
254 models to project the previously-defined HWs, the absolute value of the smallest  
255 relative bias of the previously-defined HWs in all 12 CMIP5 models is 36.66%.  
256 Comparing to their smallest relative bias, the smallest relative bias in MetUM-GOML1  
257 and MetUM-GOML2 is much smaller, indicating a better ability of MetUM-GOML1  
258 and MetUM-GOML2 in simulating the observed HWs. All the results above indicate  
259 these two models' capability of capturing the characteristics of the HWs in observations  
260 over China.

261 The good agreements in extended summer seasonal mean surface Tmax and Tmin  
262 between model simulations and observations in many aspects and the models' ability

263 of capturing the characteristics of the HWs over China suggest a fidelity of using these  
264 models for projecting their future changes. In addition, C-EP and C-PD experiments  
265 were used to investigate the decadal changes in the East Asian summer monsoon,  
266 temperature extremes over China, and HWs over China across the mid-1990s (Chen  
267 and Dong 2018; Su and Dong 2019; Tian et al. 2018). It is indicated by the previous  
268 studies that the circulation and precipitation over East Asia in present day and their  
269 decadal changes across the mid-1990s simulated by these two models are consistent  
270 with those in observations.

271 Previous studies on the HWs over China demonstrated significant observed  
272 decadal changes in frequency, intensity, and spatial pattern of the compound, daytime,  
273 and nighttime HWs over China across the mid-1990s (Chen and Li 2017; Chen and  
274 Zhai 2017; Su and Dong 2019). Su and Dong (2019) quantified that the frequency of  
275 compound HWs averaged over China in the PD almost triples that in the EP while both  
276 intensity and spatial extent are nearly doubled. In addition, their analyses also indicated  
277 that the changes of daytime and nighttime HWs are also significant in all three aspects,  
278 though not as dramatical as changes of the compound HWs. They further attributed the  
279 observed decadal changes to the changes in anthropogenic forcings. In order to compare  
280 the projected future changes in context of model simulated past decadal-multidecadal  
281 changes, the relative thresholds for three types of HWs in this study are based on early  
282 period C-EP simulations as described in above and used in Su and Dong (2019). The  
283 future changes of the HWs over China are indicated by the differences between C-FP  
284 and C-PD experiments. Statistical significance of the mean changes is assessed using a

285 two tailed Student's t-test.

## 286 **4. Future changes of HWs over China**

### 287 **4.1 Spatial patterns of future changes**

288 Fig. 3 shows the projected future changes of compound HWs over China. The  
289 frequency, intensity and duration of compound HWs significantly increase all over  
290 China, but with different spatial patterns. The increase in frequency of compound HWs  
291 over the southern part of China is greater than that over the northern part, particularly  
292 with greatest increase on the southwest fringe of mainland China, showing maximum  
293 changes of more than 5.0 events per year (Fig. 3a and b). The intensity changes of  
294 compound HWs show much larger enhancement over the northern part of China than  
295 southern part (Fig. 3c and d). The duration of compound HWs over China extends  
296 longer with the largest change (more than 3.0 days) over the southeastern China, the  
297 western China, and the southern part of northeastern China (Fig. 3e and f). Interestingly,  
298 the compound HWs over the northern China and the Tibetan Plateau show the greatest  
299 relative changes in all frequency, intensity, and duration with the largest ratios of these  
300 three features in the FP to the PD (Fig. S4), but the frequency and duration of compound  
301 HWs over the southern China are of much smaller relative changes though of the largest  
302 absolute changes (Fig. 3). The future changes of compound HWs in MetUM-GOML1  
303 and MetUM-GOML2 are consistent with each other. However, there are some slight  
304 differences between them. For instance, the increase in frequency over the northwestern  
305 China and the enhancement of intensity over northern China in MetUM-GOML2 (Fig.



306 3b, d) are a little bit stronger than those in MetUM-GOML1 (Fig. 3a, c). The high value  
307 centre of increase in duration over the southern part of China is located in the  
308 southeastern part of China in MetUM-GOML1 (Fig. 3e) but in the central southern part  
309 in MetUM-GOML2 (Fig. 3f).

310 Future changes of daytime HWs are shown in Fig. 4. All three features of daytime  
311 HWs increase significantly over most part of China. The frequency of daytime HWs  
312 increases the most over the northwestern part of China and uniformly over large part of  
313 eastern China with value of 1.0-2.0 events per year (Fig. 4a and b). The intensity of  
314 daytime HWs is enhanced more evenly than that of compound HWs with relatively  
315 high value of more than 0.6 °C/day over the southern part of China (Fig. 4c and d). The  
316 duration of daytime HWs are lengthened over most part of China, particularly with  
317 changes of more than 2.0 days being over the northwestern part of China (Fig. 4e and  
318 f). The ratios of the frequency, intensity, and duration of daytime HWs in the FP to the  
319 PD (Fig. S5) share the similar spatial patterns with the absolute changes of them (Fig.  
320 4). The future changes of daytime HWs are almost the same in the two models with  
321 very weak differences between them.

322 Future changes of nighttime HWs are illustrated in Fig. 5. Similar with the  
323 compound and daytime HWs, all three features of nighttime HWs increase significantly  
324 over China. The spatial distributions of the increase in frequency and intensity of  
325 nighttime HWs are more spatial-uniform comparing to those of the compound HWs.  
326 The increase in frequency of nighttime HWs over most part of China is similar in

327 magnitude, except the relatively large increase over the southern margin of mainland  
328 China (more than 4.0 events per year; Fig. 5a and b). The changes in intensity of  
329 nighttime HWs also show a more or less uniform increase over most part of China with  
330 value of 0.3-0.6 °C/day, apart from the greater enhancement of intensity over the  
331 northern margin of mainland China (Fig. 5c and d). The duration of nighttime HWs  
332 extends longer relatively greatly over the Tibetan Plateau and the southeast coast of  
333 China with the largest changes of more than 3.0 days over the Tibetan Plateau (Fig. 5e  
334 and f). The pattern of relative changes of nighttime HWs (Fig. S6) are similar with those  
335 of the absolute changes (Fig. 5), except that the frequency over the northeastern China  
336 and the intensity over the southern margin of mainland China show larger relative  
337 changes but smaller absolute changes, comparing to other regions. The spatial patterns  
338 of future changes of nighttime HWs in MetUM-GOML1 and MetUM-GOML2 are  
339 quite similar, despite some differences in intensity of changes, such as larger increases  
340 in frequency over the central northern China and stronger enhancement of intensity over  
341 northern margin of mainland China in MetUM-GOML2 (Fig. 5b and d).

#### 342 **4.2 Area averaged future changes**

343 Fig. 6 shows the area averaged future changes in frequency, intensity, and duration  
344 of three types of HWs over whole China and ratios of these three features in the FP  
345 projection to the PD in MetUM-GOML1 and MetUM-GOML2. The area averaged  
346 future changes and ratios of three types of HWs over China in MetUM-GOML1 in most  
347 aspects agree with those in MetUM-GOML2.

348 For compound HWs, the future changes in frequency and duration in two models  
349 are similar, but the increase in intensity in MetUM-GOML1 is slightly less than that in  
350 MetUM-GOML2. The area averaged future changes in frequency, intensity and  
351 duration of compound HWs over the whole mainland China are 3.66 (3.38) events per  
352 year, 1.45 (1.94) °C/day, and 2.53 (2.67) days in MetUM-GOML1 (MetUM-GOML2;  
353 Fig. 6a, c, and e). Compared to the compound HWs in the PD, the frequency of  
354 compound HWs increases remarkably in the FP, which is about 4-5 times the one in the  
355 PD, and the intensity and duration in the FP more or less double the ones in the PD (Fig.  
356 6b, d, and f).

357 For the daytime HWs, the changes in frequency, intensity, and duration over whole  
358 China in MetUM-GOML1 are very close to those in MetUM-GOML2, with values of  
359 1.38 events per year, 0.51 °C/day, and 0.61 days in MetUM-GOML1 relative to those  
360 ones of 1.82 events per year, 0.61 °C/day, and 0.96 days in MetUM-GOML2 (Fig. 6a,  
361 c, and e). The future changes of daytime HWs are significant but weaker than those of  
362 compound HWs. The frequency of daytime HWs in the FP increases by 60%-80%  
363 relative to that in the PD, and the intensity of daytime HWs increases by around 40%,  
364 and the duration of daytime HWs increases by 20%-30% (Fig. 6b, d, and f).

365 For the nighttime HWs, the changes in intensity over whole China are similar in  
366 two models, with value of 0.45 °C/day in MetUM-GOML1 compared to 0.58 °C/day  
367 in MetUM-GOML2 (Fig. 6c), while the changes in frequency and duration over whole  
368 China in MetUM-GOML1, with values of 2.50 events per year and 1.29 days, are about

369 3/4 of those in MetUM-GOML2, which are 3.19 events per year and 1.68 days (Fig. 6a  
370 and e). The future changes in nighttime HWs are slightly larger than those of daytime  
371 HWs, but weaker than those of compound HWs. The frequency of nighttime HWs in  
372 the FP almost doubles that in the PD, and the intensity and duration of nighttime HWs  
373 in the FP increase by about 50%-60% and 30%-50% respectively relative to those in  
374 the PD (Fig. 6b, d, and f).

375 In order to get more clarity on what these projected future changes of three types  
376 of HWs exactly mean in context of past changes, the future changes of HWs over China  
377 are compared to the past decadal changes of HWs across the mid-1990s, which are  
378 indicated by the differences between PD and EP in observations (Su and Dong 2019).  
379 Nearly all the projected future changes of the three types of HWs are stronger than their  
380 decadal changes across the mid-1990s. Specifically, the projected future changes  
381 relative to PD in frequency of compound HWs and all three aspects of daytime HWs  
382 are 2-4 times the decadal changes across the mid-1990s in observations. The future  
383 increase in duration of compound HWs and frequency and duration of nighttime HWs  
384 are 20%-80% stronger than their decadal counterparts. These results suggest people  
385 will encounter much fiercer changes of HWs over China in the near future than they  
386 have experienced across the mid-1990s.

387 Summarizing the results above, all the compound, daytime, and nighttime HWs  
388 over China are projected to occur more frequently with strengthened intensity and  
389 elongated duration in the future. Quantitatively, the increases in all three aspects of

390 compound HWs in the FP are the most remarkable with the frequency being 4-5 times  
391 that in the PD and the intensity and duration nearly doubling those in the PD. The  
392 increases in all three aspects of daytime and nighttime HWs are also considerable, with  
393 those of nighttime HWs larger than those of daytime HWs. The results of MetUM-  
394 GOML1 and MetUM-GOML2 are similar in terms of spatial patterns and area averaged  
395 quantities of the future changes in the three types of HWs over China, suggesting these  
396 projected changes are robust at least for the two models used in this study.

### 397 **4.3 Contributions of changes in mean state and variability to future changes of** 398 **HWs**

399 Changes in HWs can arise from both a shift of the temperature distribution and  
400 changes in temperature variability, such as a widening of the temperature distribution  
401 (Meehl and Tebaldi, 2004; Schar et al., 2004; Lau and Nath, 2014; Schoetter et al., 2015,  
402 Argueso et al. 2016; Guirguis et al., 2018). These studies suggested that both factors  
403 will contribute to heat wave changes in future and indicated an important role of  
404 temperature variability in shaping future HWs over North America and Europe.  
405 However, the role of shift in temperature distribution and change in temperature  
406 variability on future HWs changes over China have not studied. So, the respective  
407 contributions of them to the future changes of HWs over China projected in the two  
408 models are assessed in this subsection.

409 Fig. 7 illustrates the future changes in extended summer mean surface air  
410 temperatures. Tmax increases by more than 1.5 °C over most part of China, with three

411 high value centres of increase over the southern, northwestern, and northeastern China  
412 (Fig. 7a and b). T<sub>min</sub> increases more or less uniformly over most part of China by more  
413 than 1.5°C, but with relatively large increases over the northern margin of mainland  
414 China and relatively small increases over the southern margin of mainland China (Fig.  
415 7c and d). All these main features of changes in T<sub>max</sub> and T<sub>min</sub> are similar in both  
416 models despite some slight differences. The increase centre of T<sub>max</sub> over the southern  
417 China locates in the southeastern China in MetUM-GOML1 but in the central southern  
418 China in MetUM-GOML2 (Fig. 7a and b). The increase in T<sub>min</sub> in MetUM-GOML2  
419 is greater than that in MetUM-GOML1 over the southern and northern margins of  
420 mainland China (Fig. 7c and d). What should be mentioned, the spatial patterns of future  
421 changes of the three types of HWs are consistent with those of surface air temperatures.  
422 For instance, the increase centres of intensity and duration of compound and daytime  
423 HWs over the southern China in the two models (Fig. 3c-f and 4c-f) corresponds well  
424 with the increase centres of T<sub>max</sub> (Fig. 7a and b). The large increase in the intensity of  
425 compound and nighttime HWs over the northern margins of mainland China (Fig. 3c-  
426 d and 5c-d) coheres to the great increase in T<sub>min</sub> over that region (Fig. 7c and d).

427 To obtain the mean temperature change induced and temperature variability-  
428 change induced future changes of HWs separately, the HWs in the future related to the  
429 mean temperature changes are obtained based on constructed daily surface air  
430 temperatures (T<sub>max</sub> and T<sub>min</sub>) by adding the climatological differences in extended  
431 summer mean surface air temperatures between the C-FP and C-PD experiments (Fig.  
432 7) to daily surface air temperatures in the C-PD experiments. Then the temperature

433 variability-change induced future changes of HWs are obtained by subtracting the mean  
434 temperature change induced future changes of HWs from the total future changes of  
435 HWs, which refer to the difference between the C-FP and C-PD experiments.

436 Fig. 8 shows the total, mean temperature change induced, and temperature  
437 variability-change induced future changes of three types of HWs averaged over whole  
438 mainland China in MetUM-GOML1 and MetUM-GOML2. The future changes of HWs  
439 predominantly result from the mean temperature change, which accounts for more than  
440 79% of the total future changes. The spatial patterns of various properties in three types  
441 of HWs induced by the mean temperature change and temperature variability-change  
442 are also examined (not shown). The results of spatial patterns are consistent with the  
443 area averaged ones. The spatial patterns of the mean temperature change induced future  
444 changes of HWs are quite similar with those of the total future changes (Fig. 3-5) and  
445 the temperature variability-change induced future changes of HWs are weak and only  
446 significant over small sub-regions.

447 These results above indicate that the changes in mean temperature play a  
448 predominant role in shaping future changes of HWs over China in MetUM-GOML1  
449 and MetUM-GOML2. These are in agreement with Argueso et al. (2016) who showed  
450 that seasonal mean temperature changes control future changes in heat waves in large  
451 areas across the globe by using CMIP5 simulations. The subtle differences in future  
452 changes of HWs in the two models also result from the slight differences in future  
453 changes of mean state. The physical processes responsible for the future changes in the

454 mean surface air temperatures and subsequently the future changes of the three types  
455 of HWs are discussed in next section.

## 456 **5. Physical processes responsible for the simulated future changes of HWs**

457 The spatial patterns of future extended-summer-mean changes of some key  
458 variables in MetUM-GOML1 and MetUM-GOML2 are illustrated in Fig. 9 and 10. The  
459 main features of changes of the physical variables in the two models are similar. The  
460 most important features are increased surface downward longwave (LW) radiations  
461 everywhere (Fig. 9a and b), partly induced by the increase in GHG concentrations via  
462 the greenhouse effect and partly induced by the increase in water vapor in the  
463 atmosphere (Fig. 10a and b). The relatively large increase of downward LW radiation  
464 by about 7-9 W m<sup>-2</sup> over the eastern part of China is consistent with large increase of  
465 water vapor in the atmosphere by more than 3 kg m<sup>-2</sup>, where the moisture transport from  
466 ocean to land is enhanced (not shown) due to strengthened East Asian Summer  
467 Monsoon (EASM) and more evaporation of the ocean under the warming climate. Both  
468 the increased GHG concentrations and decreased AA emissions increase the land-sea  
469 thermal contrast by warming land more than ocean and enhance the EASM (not shown).  
470 This response of circulation is consistent with the previous studies (Lau and Kim 2017;  
471 Lau et al. 2017). The relatively large increases in surface downward LW radiation over  
472 the northern margin of China by 9-11 W m<sup>-2</sup> are mainly the direct impacts of increased  
473 greenhouse effect (Fig. 9a and b) since the increase in water vapor in the atmosphere  
474 here is relatively small than other regions (Fig. 10a and b) and land surface and



475 atmospheric feedbacks are weak due to the very dry underlying surface (Dong et al.  
476 2009).

477 The changes of net surface shortwave (SW) radiation indicate an increase over  
478 most part of China (Fig. 9c and d). This increase is contributed to by the increase of  
479 surface clear SW radiation over southeastern and northeastern China (Fig. 9e and f) and  
480 the positive anomalies of shortwave cloud radiative effect (SW CRE) over most part of  
481 China (Fig. 9g and h). The increase of surface clear SW radiation over southeastern and  
482 northeastern China is induced by the reduction of total aerosol optical depth (AOD; Fig.  
483 10c and d) through aerosol-radiation interaction, which is primarily due to the decrease  
484 of sulfur dioxide emissions (Fig. 1).

485 The positive anomalies of SW CRE over most part of China (Fig. 9g and h) result  
486 from both the decrease in cloud cover over most part of China (Fig. 10e and f) and the  
487 change of cloud radiative property due to the reduction of aerosol emissions over  
488 southeastern and northeastern China through cloud albedo effect of aerosol-cloud  
489 interaction (Twomey 1977). From the perspective of change of cloud radiative property,  
490 the decrease in aerosol emissions over southeastern and northeastern China leads to an  
491 increase in the cloud droplet size (not shown) and a decrease in the cloud droplet  
492 number concentration (not shown), resulting in the decrease in the reflectance of clouds  
493 and the positive anomalies of SW CRE relative to the high aerosol emissions during  
494 PD. From the perspective of decrease in cloud cover, different physical processes are  
495 responsible for the decreases in cloud cover over different sub-regions. Over

496 northwestern China, the reduction of cloud cover is induced by decrease in relative  
497 humidity (Fig. 10g and h), which under the global warming scenario is attributed to that  
498 water vapor in the atmosphere over land is mainly controlled by transport from ocean  
499 and constrained by ocean warming and increases less than saturation specific humidity  
500 following the Clausius-Clapeyron relationship because stronger warming over land  
501 than over ocean (e.g., Dong et al. 2009; Boé and Terray 2014). Over southeastern China,  
502 the cloud cover is decreased by cloud lifetime effect of aerosol-cloud interaction  
503 (Albrecht 1989). Over northeastern China, the reduction of cloud cover is caused by  
504 both decrease in relative humidity and cloud lifetime effect of aerosol-cloud interaction.

505 In summary, the surface air temperature during extended summer over China in  
506 the mid-21<sup>st</sup> century is raised by the increase in surface downward LW radiation related  
507 to the enhanced greenhouse effect and the increased water vapor in the atmosphere over  
508 China, resulting from the enhanced EASM and increased evaporation from ocean, and  
509 by the increase in surface SW radiation related to the decreased cloud cover over most  
510 part of China and the decreased AOD southeastern and northeastern China. These  
511 physical processes responsible for the future increases in surface air temperature over  
512 China are almost the same in MetUM-GOML1 and MetGOML2. As a result, all three  
513 aspects of compound, daytime, and nighttime HWs over China would increase in the  
514 future.

515 The slight differences in the changes of seasonal mean surface air temperature  
516 between MetUM-GOML1 and MetUM-GOML2 are induced by the differences in the

517 increase in surface SW radiation and the increase in surface downward LW radiation,  
518 which eventually lead to the subtle differences in the future changes of three types of  
519 HWs. The surface SW radiation increases more over the southeastern China in MetUM-  
520 GOML1 but over the central southern part of China in MetUM-GOML2 (Fig. 9b and  
521 c), leading to different locations of maximum Tmax change over that region (Fig. 7a  
522 and b). The surface downward LW radiation increases more over the northern margin  
523 of mainland China and central northern China in MetUM-GOML2 than in MetUM-  
524 GOML1 (Fig. 9a and b), resulting in large increase in Tmin over these regions. These  
525 differences in surface SW radiation and downward LW radiation are attributed to the  
526 slight differences in the atmospheric circulations between the two models, since the  
527 atmospheric circulations determine the aerosol distribution, water vapor transport and  
528 large-scale precipitation, which have direct or indirect effects on the energy budgets.

## 529 **6. Conclusions**

530 The future changes in the compound, daytime, and nighttime HWs over China  
531 during extended summer (May–September) in the mid-21<sup>st</sup> century (FP, 2045-2055)  
532 under RCP4.5 scenario relative to present day (PD, 1994-2011) are investigated in the  
533 aspects of frequency, intensity, and duration in this study. The numerical experiments  
534 performed by two coupled models, comprising the atmospheric components of two  
535 state-of-the-art climate models coupled to a multi-level mixed-layer ocean model and  
536 having much smaller sea surface temperature biases than fully coupled general  
537 circulation models, are used to evaluate the future changes in the HWs and to reveal the

538 physical processes associated with these changes. The principal results are concluded  
539 below.

540 The three types of HWs over China are projected to be of more frequent  
541 occurrence with strengthened intensity and elongated duration under the scenario of  
542 increased GHG concentrations and decreased aerosol emissions over Eurasian  
543 continent. The change in compound HWs will be the most dramatic in all three aspects,  
544 with the frequency in the FP being 4-5 times that in the PD, and the intensity and  
545 duration nearly doubling those in the PD. The changes of daytime and nighttime HWs  
546 are also remarkable, with the increase of nighttime HWs being larger than those of  
547 daytime HWs. The projected future changes of HWs over China are predominantly  
548 determined by the changes in seasonal mean surface air temperatures ( $T_{max}$  and  $T_{min}$ )  
549 with changes in temperature variability playing a minor role in both models.

550 The surface air temperatures are raised by increased downward LW radiation and  
551 increased surface SW radiation, which therefore increases the frequency, intensity, and  
552 duration of all three types of HWs over China. The increase in surface downward LW  
553 radiation is induced by the enhanced greenhouse effect and the increased water vapor  
554 in the atmosphere, resulting from the enhanced EASM and increased ocean evaporation  
555 in the warming climate. The increase in surface SW radiation is contributed to, partly  
556 by the decreased cloud cover due to the reduced relative humidity in a warming world  
557 and partly by the decreased aerosol emissions via direct aerosol-radiation interaction  
558 and indirect aerosol-cloud interaction over southeastern and northeastern China.

559 The future changes of the three types of HWs over China in MetUM-GOML1 and  
560 MetUM-GOML2 are consistent in terms of spatial pattern and area averaged quantities.  
561 Although slight differences exist in these future changes between two models, the  
562 projected increase in frequency, intensity, and duration of the three types of HWs over  
563 China under RCP4.5 scenario is robust among the two models used in this study.

564 Projected future changes of the three types of HWs in the mid-21<sup>st</sup> century relative  
565 to present day are stronger than their decadal changes across the mid-90s. Specifically,  
566 the projected future changes relative to PD in frequency of compound HWs and all  
567 three aspects of daytime HWs are 2-4 times of the decadal changes across the mid-  
568 1990s in observations. The future increase in duration of compound HWs and frequency  
569 and duration of nighttime HWs are 20%-80% stronger than their decadal changes across  
570 the mid-1990s. These results suggest people will encounter much fiercer changes of  
571 HWs over China in the future than they have experienced across the mid-1990s and  
572 China would face a challenge to take adaptation measures to cope with the projected  
573 frequency increase, intensity enhancement and duration lengthening of HWs.

574 The future changes of HWs over China in the mid-21<sup>st</sup> century are projected under  
575 RCP4.5 scenario in this paper. There are some other factors influencing the HWs on  
576 the other timescales. For example, the variations of western North Pacific Subtropical  
577 High, East Asian Jet Stream, and El Nino-Southern Oscillation have an impact on the  
578 interannual variability of the HWs over China (Wang et al., 2013; Wang et al., 2016;  
579 Luo and Lau, 2017; Luo and Lau, 2018). These factors should be taken into

580 consideration when forecasting the HWs on a shorter time scale.

581 **Acknowledgement**

582 This study is supported by the National Natural Science Foundation of China under  
583 Grants 41505037, 41875103, by the Applied Basic Research Foundation of Yunnan  
584 Province (2016FB078), and by the UK-China Research & Innovation Partnership Fund  
585 through the Met Office Climate Science for Service Partnership (CSSP) China as part  
586 of the Newton Fund. QS is supported by China Scholarship Council. BD is supported  
587 by the U.K. National Centre for Atmospheric Science-Climate (NCAS-Climate) at the  
588 University of Reading. The authors like to thank three anonymous reviewers for their  
589 constructive comments on the earlier version of the paper.

590

591 **Reference**

- 592 Albrecht, B. A. (1989) Aerosols, cloud microphysics, and fractional cloudiness. *Science*,  
593 **245**(4923), 1227-1230, <https://doi.org/10.1126/science.245.4923.1227>.
- 594 Argueso, D., A. Di Luca, S. E. Perkins- Kirkpatrick and J. P. Evans (2016) Seasonal  
595 mean temperature changes control future heat waves. *Geophys. Res. Lett.*, **43**(14),  
596 7653-7660, <https://doi.org/10.1002/2016GL069408>.
- 597 Arribas, A., M. Glover, A. Maidens, K. Peterson, M. Gordon, C. MacLachlan, R.  
598 Graham, D. Fereday, J. Camp and A. Scaife (2011) The GloSea4 ensemble  
599 prediction system for seasonal forecasting. *Mon. Wea. Rev.*, **139**(6), 1891-1910,  
600 <https://doi.org/10.1175/2010MWR3615.1>.
- 601 Black, E., M. Blackburn, G. Harrison, B. Hoskins and J. Methven (2004) Factors  
602 contributing to the summer 2003 European heatwave. *Weather*, **59**(8), 217-223,  
603 <https://doi.org/doi:10.1256/wea.74.04>.
- 604 Boé, J. and L. Terray (2014) Land–sea contrast, soil-atmosphere and cloud-temperature  
605 interactions: interplays and roles in future summer European climate change. *Clim.*  
606 *Dyn.*, **42**(3-4), 683-699, <https://doi.org/10.1007/s00382-013-1868-8>.
- 607 Chen, R. D. and R. Y. Lu (2014) Large-scale circulation anomalies associated with  
608 'tropical night' weather in Beijing, China. *Int. J. Climatol.*, **34**(6), 1980-1989,  
609 <https://doi.org/10.1002/joc.3815>.
- 610 Chen, W. and B. Dong (2018) Anthropogenic impacts on recent decadal change in  
611 temperature extremes over China: relative roles of greenhouse gases and  
612 anthropogenic aerosols. *Clim. Dyn.*, <https://doi.org/10.1007/s00382-018-4342-9>.
- 613 Chen Y., W. Chen, Q. Su, F. Luo, S. Sparrow, F. Tian, B. Dong, S. F. B. Tett, F. C. Lott,  
614 and D. Wallom (2018) Anthropogenic warming has substantially increased the  
615 likelihood of July 2017-like heat waves over Central-Eastern China [in  
616 "Explaining Extremes of 2017 from a Climate Perspective"]. Accepted by *Bull.*  
617 *Amer. Meteor. Soc.*.
- 618 Chen, Y. and Y. Li (2017) An inter-comparison of three heat wave types in China during  
619 1961-2010: Observed basic features and linear trends. *Sci. Rep.*, **7**, 45619,  
620 <https://doi.org/10.1038/srep45619>.
- 621 Chen, Y. and P. Zhai (2017) Revisiting summertime hot extremes in China during  
622 1961- 2015: overlooked compound extremes and significant changes. *Geophys.*  
623 *Res. Lett.*, **44**(10), <https://doi.org/10.1002/2016GL072281>.
- 624 Coumou, D. and S. Rahmstorf (2012) A decade of weather extremes. *Nat. Clim. Change*,  
625 **2**(7), 491-496, <https://doi.org/10.1038/nclimate1452>.
- 626 Della-Marta, P. M., J. Luterbacher, H. von Weissenfluh, E. Xoplaki, M. Brunet and H.  
627 Wanner (2007) Summer heat waves over western Europe 1880–2003, their  
628 relationship to large-scale forcings and predictability. *Clim. Dyn.*, **29**(2), 251-275,

- 629 <https://doi.org/10.1007/s00382-007-0233-1>.
- 630 Dong, B., J. M. Gregory and R. T. Sutton (2009) Understanding land–sea warming  
631 contrast in response to increasing greenhouse gases. Part I: Transient adjustment.  
632 *J. Clim.*, **22**(11), 3079-3097, <https://doi.org/10.1175/2009JCLI2652.1>.
- 633 Dong, B., R. T. Sutton, L. Shaffrey and N. P. Klingaman (2017) Attribution of forced  
634 decadal climate change in coupled and uncoupled ocean–atmosphere model  
635 experiments. *J. Clim.*, **30**(16), 6203-6223, <https://doi.org/10.1175/jcli-d-16-0578.1>.
- 637 Freychet, N., S. Tett, J. Wang and G. Hegerl (2017) Summer heat waves over Eastern  
638 China: dynamical processes and trend attribution. *Environ. Res. Lett.*, **12**(2),  
639 024015, <https://doi.org/10.1088/1748-9326/aa5ba3>.
- 640 Freychet, N., S. Sparrow, S. F. B. Tett, M. J. Mineter, G. C. Hegerl and D. C. H. Wallom  
641 (2018) Impacts of anthropogenic forcings and El Nino on Chinese extreme  
642 temperatures. *Adv. Atmos. Sci.*, **35**(8), 994-1002, <https://doi.org/10.1007/s00376-018-7258-8>.
- 644 Gershunov, A., D. R. Cayan and S. F. Iacobellis (2009) The great 2006 heat wave over  
645 California and Nevada: signal of an increasing trend. *J. Clim.*, **22**(23), 6181-6203,  
646 <https://doi.org/10.1175/2009JCLI2465.1>.
- 647 Guirguis, K., A. Gershunov, D. R. Cayan and D. W. Pierce (2018) Heat wave  
648 probability in the changing climate of the Southwest US. *Clim. Dyn.*, **50**(9-10),  
649 3853-3864, <https://doi.org/10.1007/s00382-017-3850-3>.
- 650 Gosling, S. N., J. A. Lowe, G. R. McGregor, M. Pelling and B. D. Malamud (2009)  
651 Associations between elevated atmospheric temperature and human mortality: a  
652 critical review of the literature. *Climatic Change*, **92**(3-4), 299-341,  
653 <https://doi.org/10.1007/s10584-008-9441-x>.
- 654 Guo, X., J. Huang, Y. Luo, Z. Zhao and Y. Xu (2017) Projection of heat waves over  
655 China for eight different global warming targets using 12 CMIP5 models. *Theor.*  
656 *Appl. Climatol.*, **128**(3-4), 507-522, <https://doi.org/10.1007/s00704-015-1718-1>.
- 657 Hatfield, J. L. and J. H. Prueger (2015) Temperature extremes: Effect on plant growth  
658 and development. *Weather and Climate Extremes*, **10**, 4-10,  
659 <https://doi.org/10.1016/j.wace.2015.08.001>.
- 660 Hirons, L., N. Klingaman and S. Woolnough (2015) MetUM-GOML: a near-globally  
661 coupled atmosphere–ocean-mixed-layer model. *Geosci. Model Dev.*, **8**, 363-379,  
662 <https://doi.org/10.5194/gmd-8-363-2015>.
- 663 Jones, C., et al (2011) The HadGEM2-ES implementation of CMIP5 centennial  
664 simulations. *Geosci. Model Dev.*, **4**(3), 543–570, <https://doi.org/10.5194/gmd-4-543-2011>.
- 666 Karl, T. R. and R. W. Knight (1997) The 1995 Chicago heat wave: How likely is a



- 667 recurrence? *Bull. Amer. Meteor. Soc.*, **78**(6), 1107-1120,  
668 [https://doi.org/10.1175/1520-0477\(1997\)078<1107:tchwhl>2.0.co;2](https://doi.org/10.1175/1520-0477(1997)078<1107:tchwhl>2.0.co;2).
- 669 Lamarque, J.-F., G. P. Kyle, M. Meinshausen, K. Riahi, S. J. Smith, D. P. van Vuuren,  
670 A. J. Conley and F. Vitt (2011) Global and regional evolution of short-lived  
671 radiatively-active gases and aerosols in the Representative Concentration  
672 Pathways. *Climatic Change*, **109**, 191, [https://doi.org/10.1007/s10584-011-0155-](https://doi.org/10.1007/s10584-011-0155-0)  
673 [0](https://doi.org/10.1007/s10584-011-0155-0).
- 674 Lamarque, J.-F., T. C. Bond, V. Eyring, C. Granier, A. Heil, Z. Klimont, D. Lee, C.  
675 Liousse, A. Mieville and B. Owen (2010) Historical (1850–2000) gridded  
676 anthropogenic and biomass burning emissions of reactive gases and aerosols:  
677 methodology and application. *Atmos. Chem. Phys.*, **10**(15), 7017-7039,  
678 <https://doi.org/10.5194/acp-10-7017-2010>.
- 679 Lau, N.-C., and M. J. Nath (2014) Model simulation and projection of European heat  
680 waves in present-day and future climates, *J. Clim.*, **27**(10), 3713–3730,  
681 <https://doi.org/10.1175/jcli-d-13-00284.1>.
- 682 Lau, W. K. M., K. M. Kim and L. R. Leung (2017) Changing circulation structure and  
683 precipitation characteristics in Asian monsoon regions: greenhouse warming vs.  
684 aerosol effects. *Geosci. Lett.*, **4**(1), 28, [https://doi.org/10.1186/s40562-017-0094-](https://doi.org/10.1186/s40562-017-0094-3)  
685 [3](https://doi.org/10.1186/s40562-017-0094-3).
- 686 Lau, W. K. M. and K. M. Kim (2017) Competing influences of greenhouse warming  
687 and aerosols on Asian summer monsoon circulation and rainfall. *Asia-Pac. J. Atmo.*  
688 *Sci.*, **53**(2), 181-194, <https://doi.org/10.1007/s13143-017-0033-4>.
- 689 Lesk, C., P. Rowhani and N. Ramankutty (2016) Influence of extreme weather disasters  
690 on global crop production. *Nature*, **529**(7584), 84,  
691 <https://doi.org/10.1038/nature16467>.
- 692 Li, Y., Y. Ding and W. Li (2017) Observed trends in various aspects of compound heat  
693 waves across China from 1961 to 2015. *J. Meteor. Res.*, **31**(3), 455-467,  
694 <https://doi.org/10.1007/s13351-017-6150-2>.
- 695 Li, Z., L. J. Cao, Y. N. Zhu and Z. W. Yan (2016) Comparison of two homogenized  
696 datasets of daily maximum/mean/minimum temperature in China during 1960-  
697 2013. *J. Meteor. Res.*, **30**(1), 53-66, <https://doi.org/10.1007/s13351-016-5054-x>.
- 698 Luo, F., B. Dong, F. Tian and S. Li (2018). Anthropogenically forced decadal change  
699 of South Asian summer monsoon across the mid-1990s. Submitted to *J. Geophys.*  
700 *Res. Atmos.*.
- 701 Luo, M. and N.-C. Lau (2017) Heat waves in southern China: Synoptic behavior, long-  
702 term change, and urbanization effects. *J. Clim.*, **30**(2), 703-720,  
703 <https://doi.org/10.1175/jcli-d-16-0269.1>.
- 704 Luo, M. and N.-C. Lau (2018) Synoptic characteristics, atmospheric controls, and long-  
705 term changes of heat waves over the Indochina Peninsula. *Clim. Dyn.*, **51**(7-8),

706 2707-2723, <https://doi.org/10.1007/s00382-017-4038-6>.

707 Ma, S. M., T. J. Zhou, D. A. Stone, O. Angelil and H. Shiogama (2017) Attribution of  
708 the July-August 2013 heat event in Central and Eastern China to anthropogenic  
709 greenhouse gas emissions. *Environ. Res. Lett.*, **12**(5),  
710 <https://doi.org/10.1088/1748-9326/aa69d2>.

711 Meehl, G. A. and C. Tebaldi (2004) More intense, more frequent, and longer lasting  
712 heat waves in the 21st Century. *Science*, **305**(5686), 994-997,  
713 <https://doi.org/10.1126/science.1098704>.

714 Moss, R. H., J. A. Edmonds, K. A. Hibbard, M. R. Manning, S. K. Rose, D. P. Vuuren,  
715 Van, T. R. Carter, E. Seita, K. Mikiko and K. Tom (2010) The next generation of  
716 scenarios for climate change research and assessment. *Nature*, **463**(7282), 747-  
717 756, <https://doi.org/10.1038/nature08823>.

718 Perkins, S. E. (2015) A review on the scientific understanding of heatwaves—Their  
719 measurement, driving mechanisms, and changes at the global scale. *Atmos. Res.*,  
720 **164–165**, 242-267, <https://doi.org/10.1016/j.atmosres.2015.05.014>.

721 Perkins, S. E. and L. V. Alexander (2013) On the measurement of heat waves. *J. Clim.*,  
722 **26**(13), 4500-4517, <https://doi.org/10.1175/jcli-d-12-00383.1>.

723 Rayner NA, Parker DE, Horton EB, Folland CK, Alexander LV, Rowell DP, Kent EC,  
724 Kaplan A (2003) Global analyses of SST, sea ice and night marine air temperature  
725 since the late nineteenth century. *J Geophys Res* 108. doi:10.1029/2002JD002670

726 Robine, J.-M., S. L. K. Cheung, S. Le Roy, H. Van Oyen, C. Griffiths, J.-P. Michel and  
727 F. R. Herrmann (2008) Death toll exceeded 70,000 in Europe during the summer  
728 of 2003. *C. R. Biol.*, **331**(2), 171-178, <https://doi.org/10.1016/j.crv.2007.12.001>.

729 Seneviratne, S. I., M. G. Donat, B. Mueller and L. V. Alexander (2014) No pause in the  
730 increase of hot temperature extremes. *Nat. Clim. Change*, **4**(3), 161,  
731 <https://doi.org/10.1038/nclimate2145>.

732 Schär, C., P. L. Vidale, D. Lüthi, C. Frei, C. Häberli, M. A. Liniger, and C. Appenzeller  
733 (2004), The role of increasing temperature variability in European summer  
734 heatwaves, *Nature*, **427**(6972), 332–336, <https://doi.org/10.1038/nature02300>.

735 Schoetter, R., J. Cattiaux and H. Douville (2015) Changes of western European heat  
736 wave characteristics projected by the CMIP5 ensemble. *Clim. Dyn.*, **45**(5-6), 1601-  
737 1616, <https://doi.org/10.1007/s00382-014-2434-8>.

738 Smith, D. M. and J. M. Murphy (2007) An objective ocean temperature and salinity  
739 analysis using covariances from a global climate model. *J. Geophys. Res. Oceans*,  
740 **112**(C2), <https://doi.org/10.1029/2005JC003172>.

741 Sparrow, S., Q. Su, F. X. Tian, S. H. Li, Y. Chen, W. Chen, F. F. Luo, N. Freychet, F. C.  
742 Lott, B. W. Dong, S. F. B. Tett and D. Wallom (2018) Attributing human influence  
743 on the July 2017 Chinese heatwave: the influence of sea-surface temperatures.

- 744 *Environ. Res. Lett.*, **13**(11), <https://doi.org/10.1088/1748-9326/ade356>.
- 745 Stefanon, M., D. A. Fabio and D. Philippe (2012) Heatwave classification over Europe  
746 and the Mediterranean region. *Environ. Res. Lett.*, **7**(1), 014023,  
747 <https://doi.org/10.1088/1748-9326/7/1/014023>.
- 748 Su, Q. and B. Dong (2019) Recent decadal changes in heat waves over China: drivers  
749 and mechanisms. Submitted to *J. Clim.*.
- 750 Sun, Y., L. Song, H. Yin, B. Zhou, T. Hu, X. Zhang and P. Stott (2016) Human influence  
751 on the 2015 extreme high temperature events in Western China [in "Explaining  
752 Extremes of 2015 from a Climate Perspective"]. *Bull. Amer. Meteor. Soc.*, **97**(12),  
753 S102-S106, <https://doi.org/10.1175/bams-d-16-0158.1>.
- 754 Sun, Y., X. B. Zhang, F. W. Zwiers, L. C. Song, H. Wan, T. Hu, H. Yin and G. Y. Ren  
755 (2014) Rapid increase in the risk to extreme summer heat in Eastern China. *Nat.*  
756 *Clim. Change*, **4**(12), 1082-1085, <https://doi.org/10.1038/nclimate2410>.
- 757 Tan, J., Y. Zheng, G. Song, L. S. Kalkstein, A. J. Kalkstein and X. Tang (2007) Heat  
758 wave impacts on mortality in Shanghai, 1998 and 2003. *Int. J. Biometeorol.*, **51**(3),  
759 193-200, <https://doi.org/10.1007/s00484-006-0058-3>.
- 760 Tian, F., B. Dong, J. Robson and R. Sutton (2018) Forced decadal changes in the East  
761 Asian summer monsoon: the roles of greenhouse gases and anthropogenic aerosols.  
762 *Clim. Dyn.*, 1-17, <https://doi.org/10.1007/s00382-018-4105-7>.
- 763 Twomey, S. (1977) Influence of pollution on shortwave albedo of clouds. *J. Atmos. Sci.*,  
764 **34**(7), 1149-1152, [https://doi.org/10.1175/1520-0469\(1977\)034<1149:tiopot>2.0.co;2](https://doi.org/10.1175/1520-0469(1977)034<1149:tiopot>2.0.co;2).
- 766 Walters, D., M. Best, A. Bushell, D. Copey, J. Edwards, P. Falloon, C. Harris, A. Lock,  
767 J. Manners and C. Morcrette (2011) The Met Office Unified Model global  
768 atmosphere 3.0/3.1 and JULES global land 3.0/3.1 configurations. *Geosci. Model*  
769 *Dev.*, **4**(4), 919, <https://doi.org/10.5194/gmd-4-919-2011>.
- 770 Walters, D., N. Wood, S. Vosper and S. Milton (2014) ENDGame: A new dynamical  
771 core for seamless atmospheric prediction. Met Office documentation, can be  
772 consulted at  
773 <http://www.metoffice.gov.uk/media/pdf/s/h/ENDGameGOVSciv2.0.pdf>.
- 774 Walters, D., M. Brooks, I. Boutle, T. Melvin, R. Stratton, S. Vosper, H. Wells, K.  
775 Williams, N. Wood and T. Allen (2017) The Met Office unified model global  
776 atmosphere 6.0/6.1 and JULES global land 6.0/6.1 configurations. *Geosci. Model*  
777 *Dev.*, **10**(4), 1487-1520, <https://doi.org/10.5194/gmd-10-1487-2017>.
- 778 Wang, C., L. Zhang, S.-K. Lee, L. Wu, and C. R. Mechoso (2014) A global perspective  
779 on CMIP5 climate model biases. *Nat. Clim. Change*, **4**, 201–205,  
780 doi:<https://doi.org/10.1038/nclimate2118>.
- 781 Wang, P., J. Tang, X. Sun, S. Wang, J. Wu, X. Dong and J. Fang (2017) Heatwaves in

- 782 China: definitions, leading patterns and connections to large-scale atmospheric  
783 circulation and SSTs. *J. Geophys. Res. Atmos.*, **122**(20),  
784 <https://doi.org/10.1002/2017JD027180>.
- 785 Wang, W., W. Zhou, X. Li, X. Wang and D. Wang (2016) Synoptic-scale characteristics  
786 and atmospheric controls of summer heat waves in China. *Clim. Dyn.*, **46**(9), 2923-  
787 2941, <https://doi.org/10.1007/s00382-015-2741-8>.
- 788 Wang, W., W. Zhou, X. Wang, S. K. Fong and K. C. Leong (2013) Summer high  
789 temperature extremes in Southeast China associated with the East Asian jet stream  
790 and circumglobal teleconnection. *J. Geophys. Res. Atmos.*, **118**(15), 8306-8319,  
791 <https://doi.org/10.1002/jgrd.50633>.
- 792 Wilbanks, T. J. and S. Fernandez (2014) Climate change and infrastructure, urban  
793 systems, and vulnerabilities: Technical report for the US department of energy in  
794 support of the national climate assessment, Island Press.
- 795 Wilcox, L. J., B. Dong, R. T. Sutton and E. J. Highwood (2015) The 2014 hot, dry  
796 summer in Northeast Asia [in "Explaining Extremes of 2014 from a Climate  
797 Perspective"]. *Bull. Amer. Meteor. Soc.*, **96**(12), S105-S110,  
798 <https://doi.org/10.1175/bams-d-15-00123.1>.
- 799 You, Q. L., Z. H. Jiang, L. Kong, Z. W. Wu, Y. T. Bao, S. C. Kang and N. Pepin (2017)  
800 A comparison of heat wave climatologies and trends in China based on multiple  
801 definitions. *Clim. Dyn.*, **48**(11), 3975-3989, [https://doi.org/10.1007/s00382-016-](https://doi.org/10.1007/s00382-016-3315-0)  
802 [3315-0](https://doi.org/10.1007/s00382-016-3315-0).
- 803 Yu, R., P. M. Zhai and Y. Y. Lu (2018) Implications of differential effects between 1.5  
804 and 2 degrees C global warming on temperature and precipitation extremes in  
805 China's urban agglomerations. *Int. J. Climatol.*, **38**(5), 2374-2385,  
806 <https://doi.org/10.1002/joc.5340>.
- 807 Zhou, B., Q. H. Wen, Y. Xu, L. Song and X. Zhang (2014a) Projected changes in  
808 temperature and precipitation extremes in China by the CMIP5 multimodel  
809 ensembles. *J. Clim.*, **27**(17), 6591-6611, <https://doi.org/10.1175/jcli-d-13-00761.1>.
- 810 Zhou, T. J., S. M. Ma and L. W. Zou (2014b) Understanding a hot summer in Central  
811 Eastern China: summer 2013 in context of multimodel trend analysis [in  
812 "Explaining Extremes of 2013 from a Climate Perspective"]. *Bull. Amer. Meteor.*  
813 *Soc.*, **95**(9), S54-S57.

814

815 **Table 1.** Summary of numerical experiments

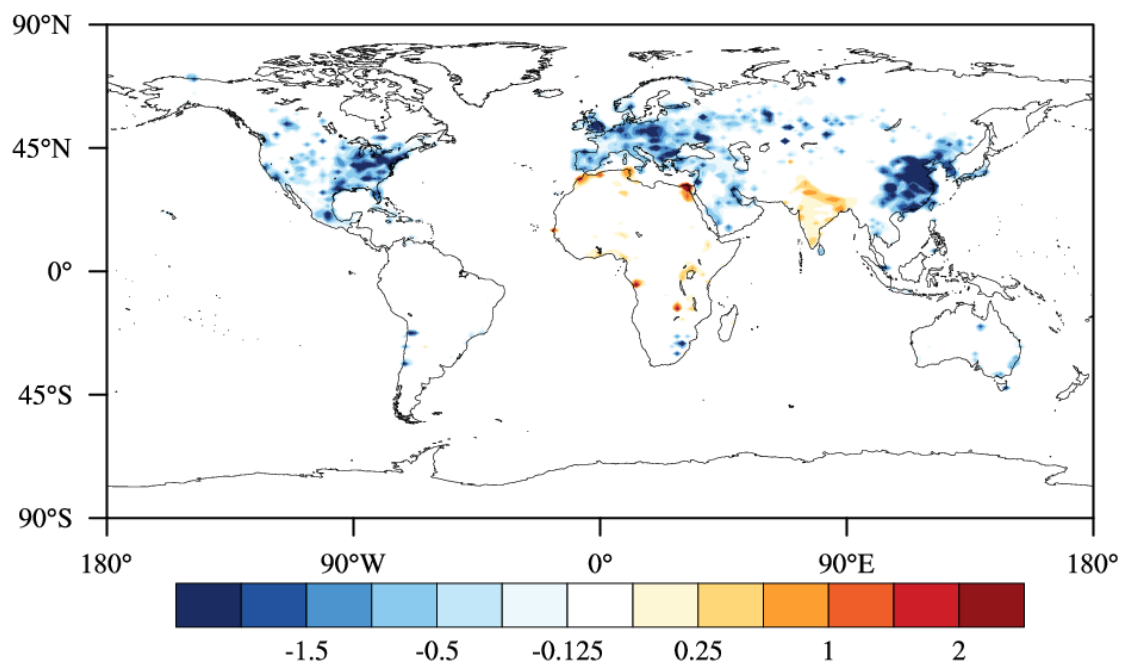
<b>Abv.</b>	<b>Experiment</b>	<b>Ocean</b>	<b>Radiative forcing</b>
<b>R0</b>	Relaxation run	Relaxation to “present day” (PD, 1994-2011) mean 3D ocean temperature and salinity to diagnose climatological temperature and salinity tendencies	PD greenhouse gases (GHGs) over 1994~2011 and anthropogenic aerosol (AA) emissions over 1994~2010 with AA after 2006 from RCP4.5 scenario (Lamarque et al. 2010, 2011)
<b>C-EP</b>	Early period (EP 1964~1981)	Climatological temperature and salinity tendencies from relaxation run	EP mean GHG and EP mean AA emissions
<b>C-PD</b>	Present day (PD 1994~2011)		PD mean GHG and PD mean AA emissions
<b>C-FP</b>	future period (FP, 2045-2055)		RCP4.5 emission scenario

816

817

818

### Annual sulfur dioxide (2045-2055 minus 1994-2010)

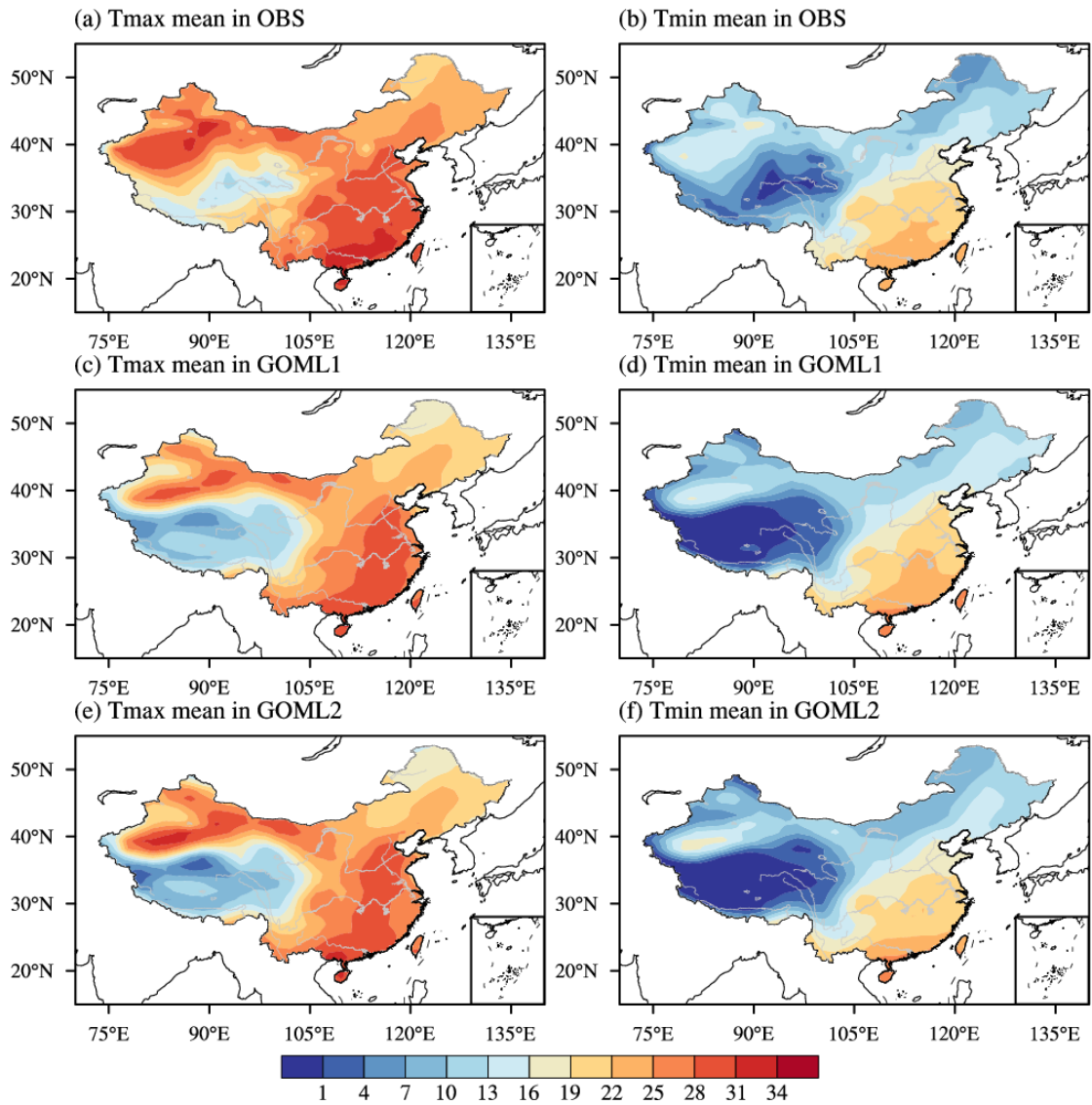


819

820 **Figure 1.** Future changes in annual mean sulfur dioxide emissions (units:  $\text{g m}^{-2} \text{yr}^{-1}$ ) during the

821 mid-21<sup>st</sup> century relative to the PD of 1994-2010.

822



823

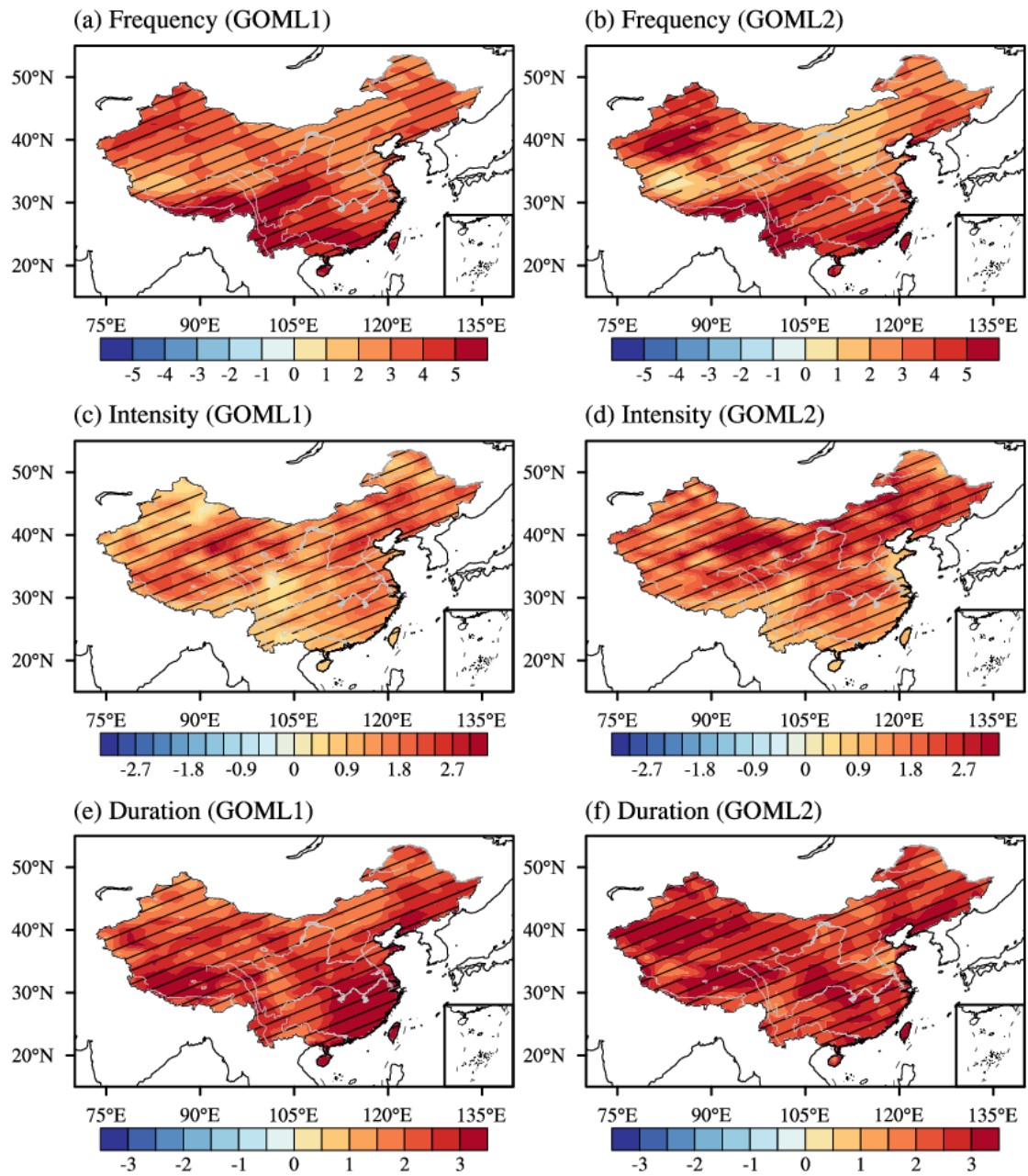
824 **Figure 2.** Climatological means of extended-summer-mean (May–September) Tmax and Tmin

825 during the EP (1964-1981) in observations (a and b) and in the C-EP experiment of MetUM-

826 GOML1 (c and d) and MetUM-GOML2 (e and f). Units are in °C.

827

## Compound HWs



828

829 **Figure 3.** Spatial patterns of future changes in frequency (units: events/year; a and b), intensity

830 (units: °C/day; c and d), and duration (units: days; e and f) of compound HWs in MetUM-GOML1

831 (left panels) and MetUM-GOML2 (right panels), masked by China boundary. The slashes highlight

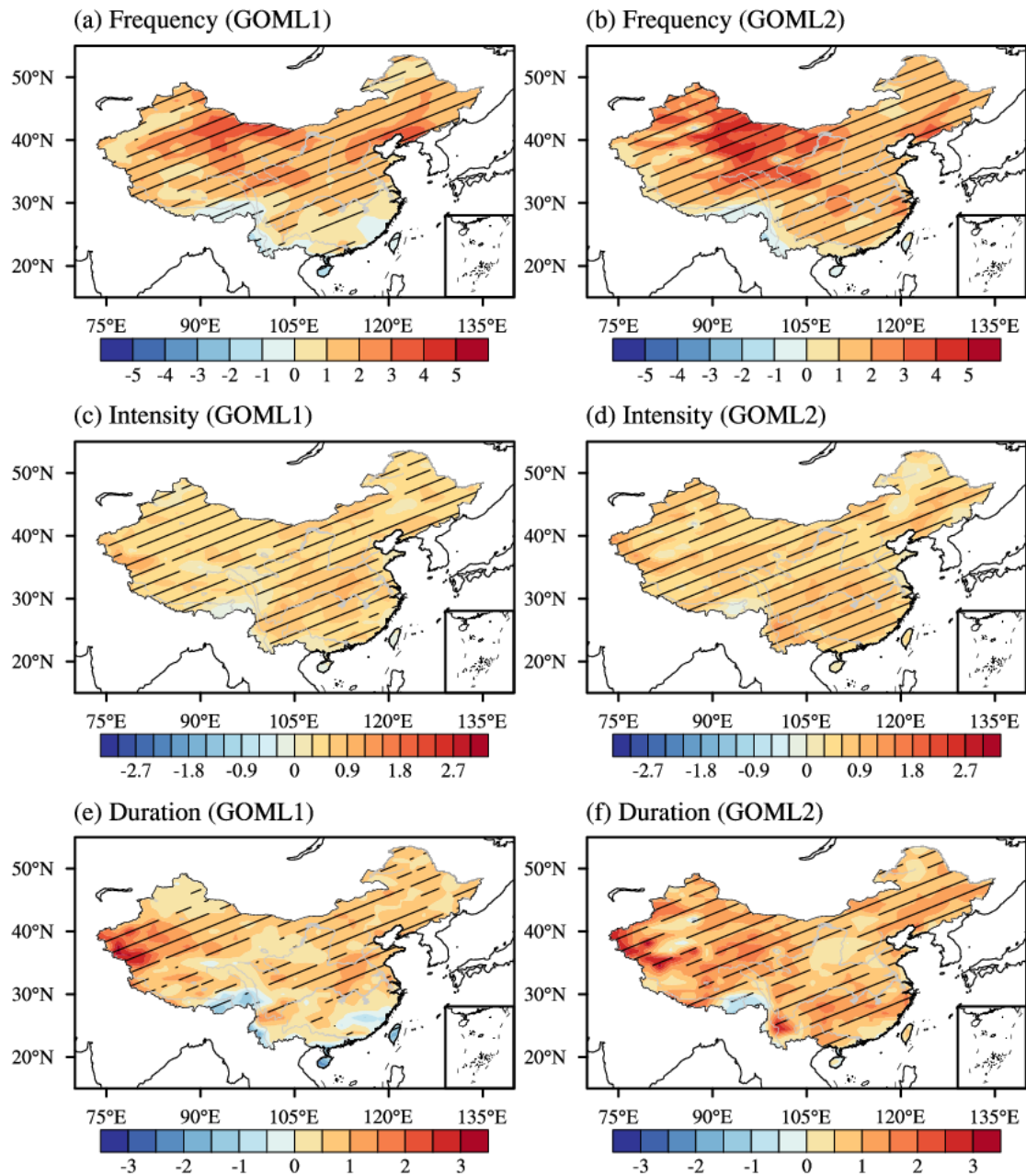
832 the regions where the differences are statistically significant at the 90% confidence level based on

833 a two-tailed Student's *t*-test.

834



## Daytime HWs



835

836 **Figure 4.** Spatial patterns of future changes in frequency (units: events/year; a and b), intensity

837 (units: °C/day; c and d), and duration (units: days; e and f) of daytime HWs in MetUM-GOML1

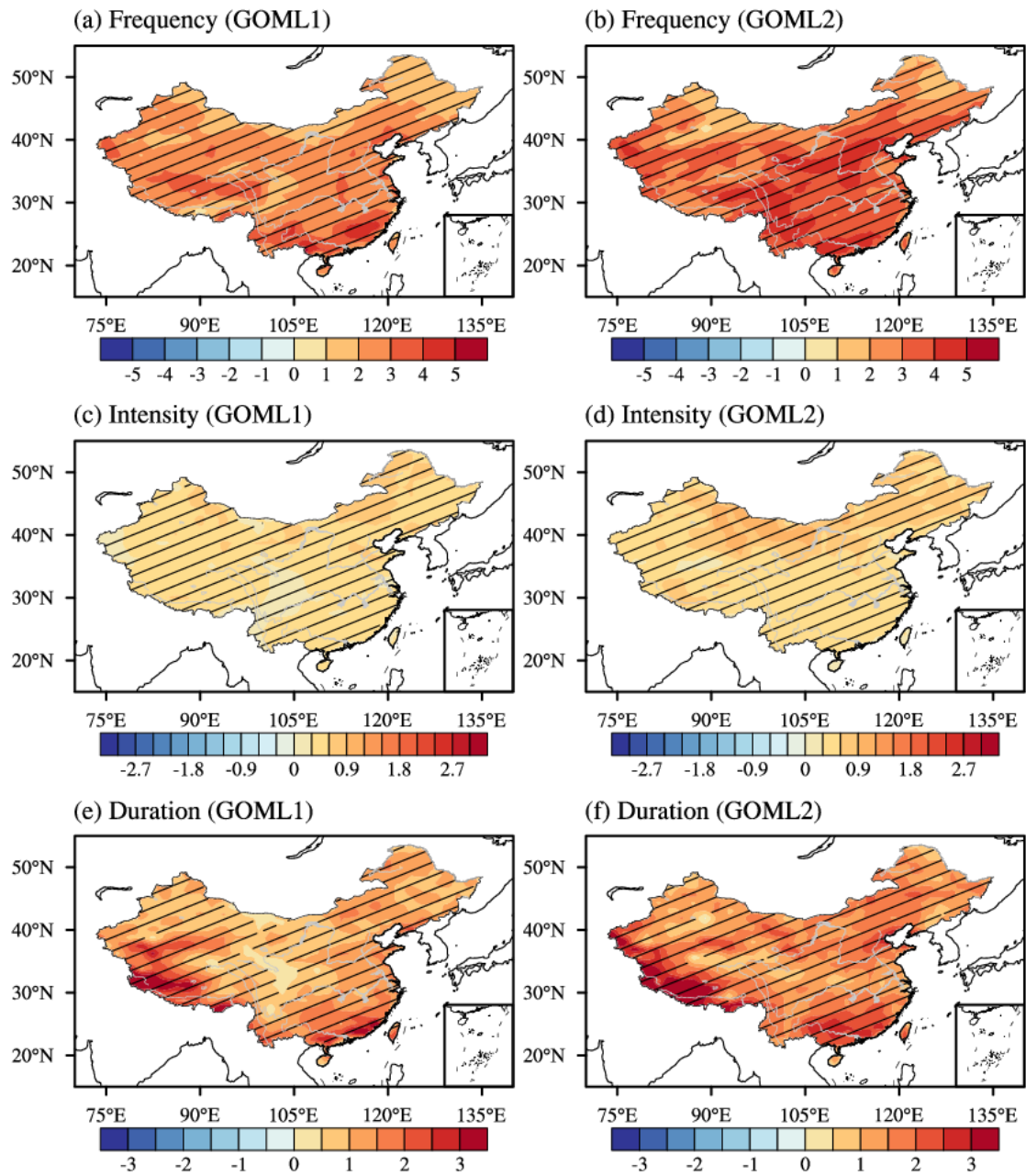
838 (left panels) and MetUM-GOML2 (right panels), masked by China boundary. The slashes highlight

839 the regions where the differences are statistically significant at the 90% confidence level based on

840 a two-tailed Student's *t*-test.

841

## Nighttime HWs



842

843 **Figure 5.** Spatial patterns of future changes in frequency (units: events/year; a and b), intensity

844 (units: °C/day; c and d), and duration (units: days; e and f) of nighttime HWs in MetUM-GOML1

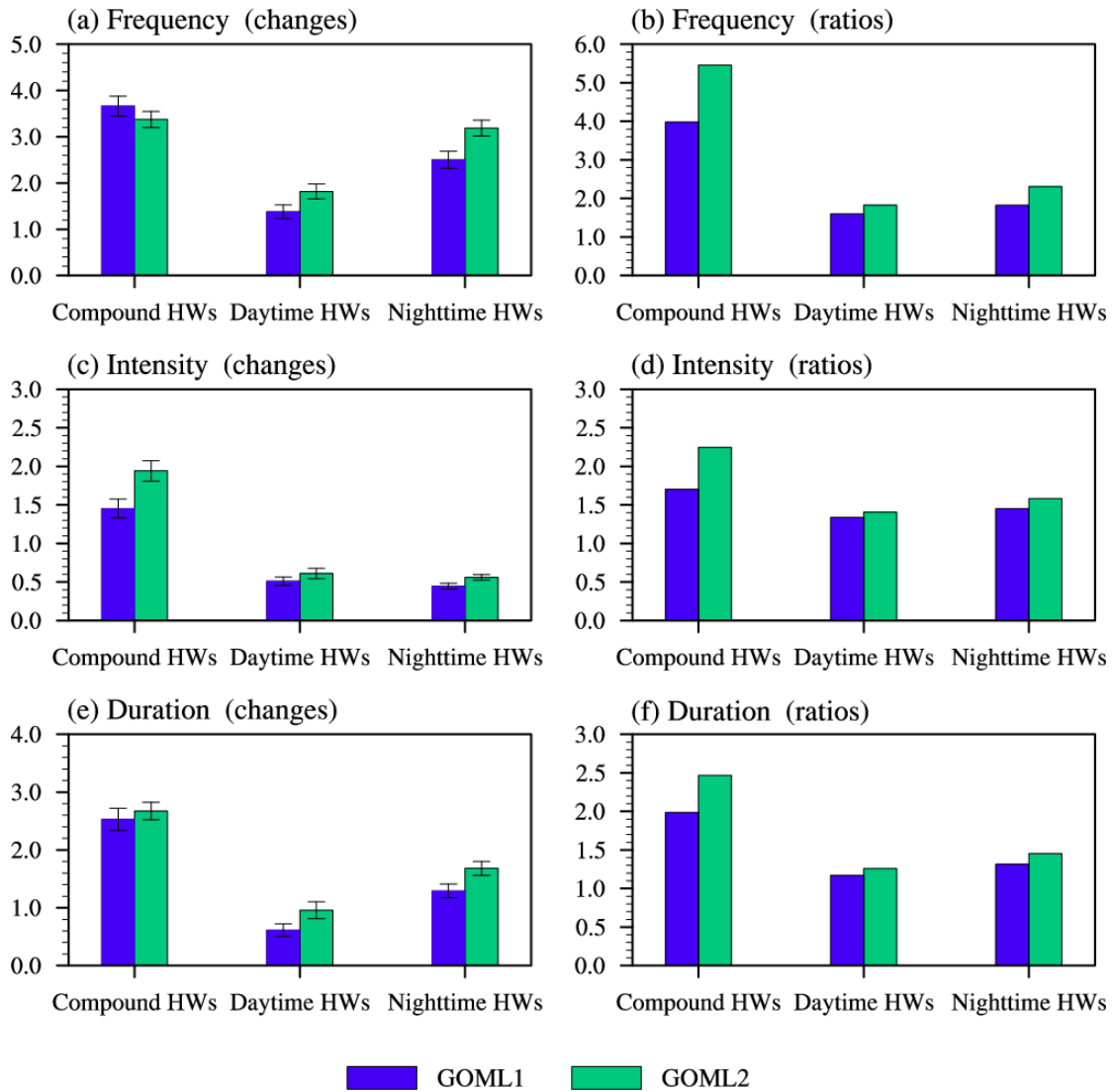
845 (left panels) and MetUM-GOML2 (right panels), masked by China boundary. The slashes highlight

846 the regions where the differences are statistically significant at the 90% confidence level based on

847 a two-tailed Student's *t*-test.

848

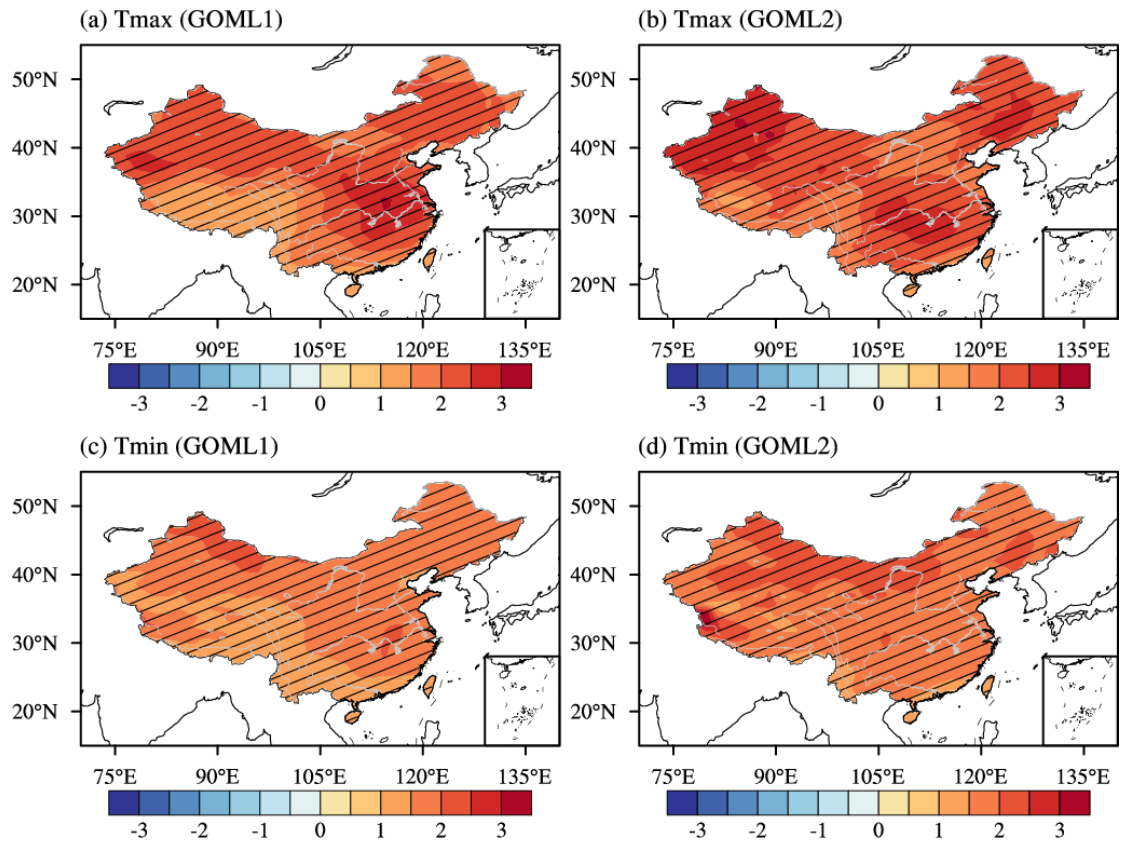
849



850

GOML1 GOML2

851 **Figure 6.** Area averaged future changes of frequency (a), intensity (c), and duration (e) of compound,  
 852 daytime, and nighttime HWs over whole China and the ratios of these three features in the FP  
 853 projection to the PD (b, d, and f) in MetUM-GOML1 and MetUM-GOML2. Units for frequency,  
 854 intensity, and duration are events/year, °C/day, and days, respectively. The error bars indicate the  
 855 90% confidence intervals based on two-tailed Student's *t*-test.



856

857 **Figure 7.** Future changes in the extended-summer-mean (May–September) Tmax and Tmin relative

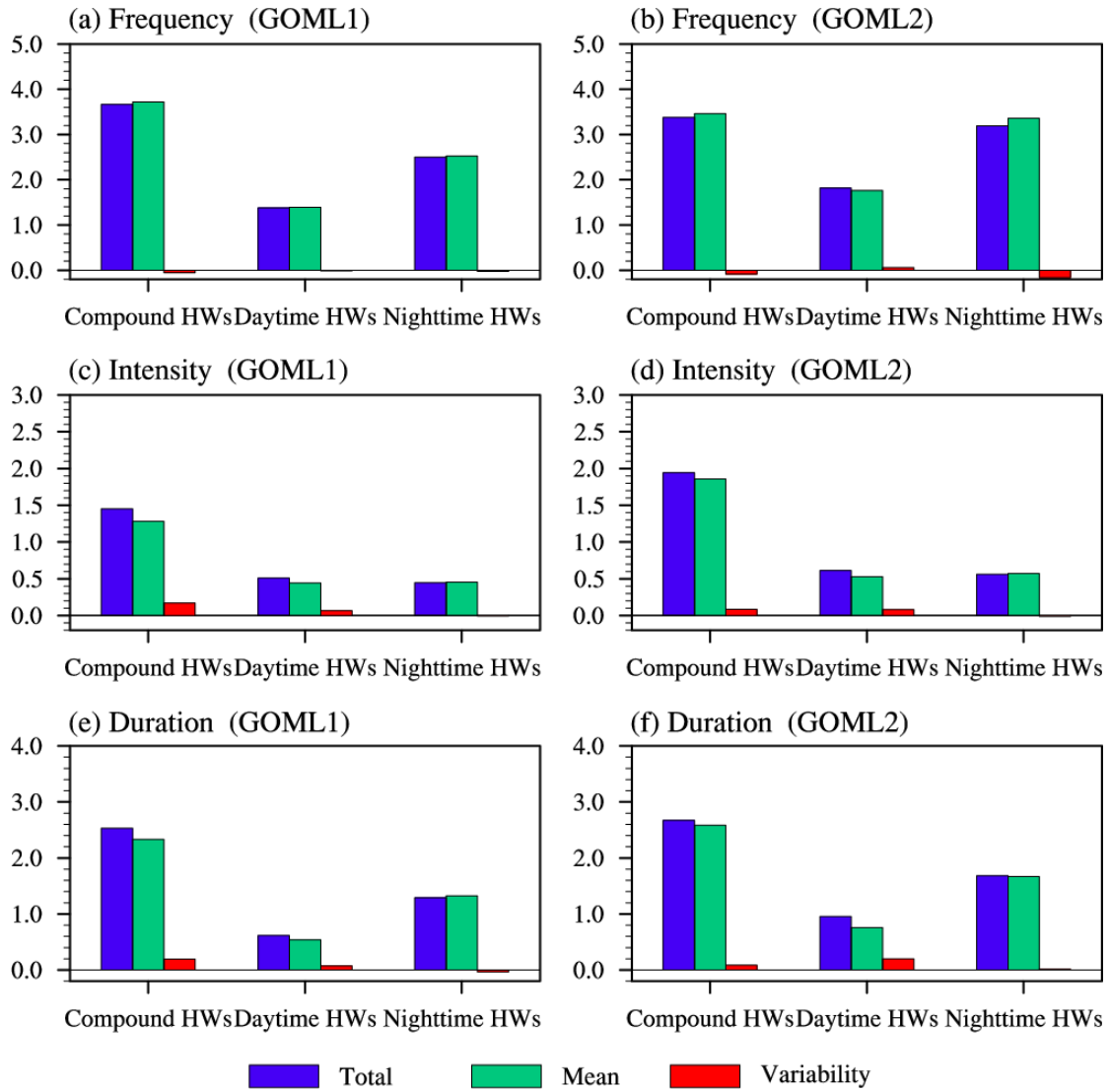
858 to PD simulations in MetUM-GOML1 (a and c) and MetUM-GOML2 (b and d). Units are in °C.

859 The slashes highlight the regions where the differences are statistically significant at the 90%

860 confidence level based on a two-tailed Student's *t*-test.

861

862



863

864

865

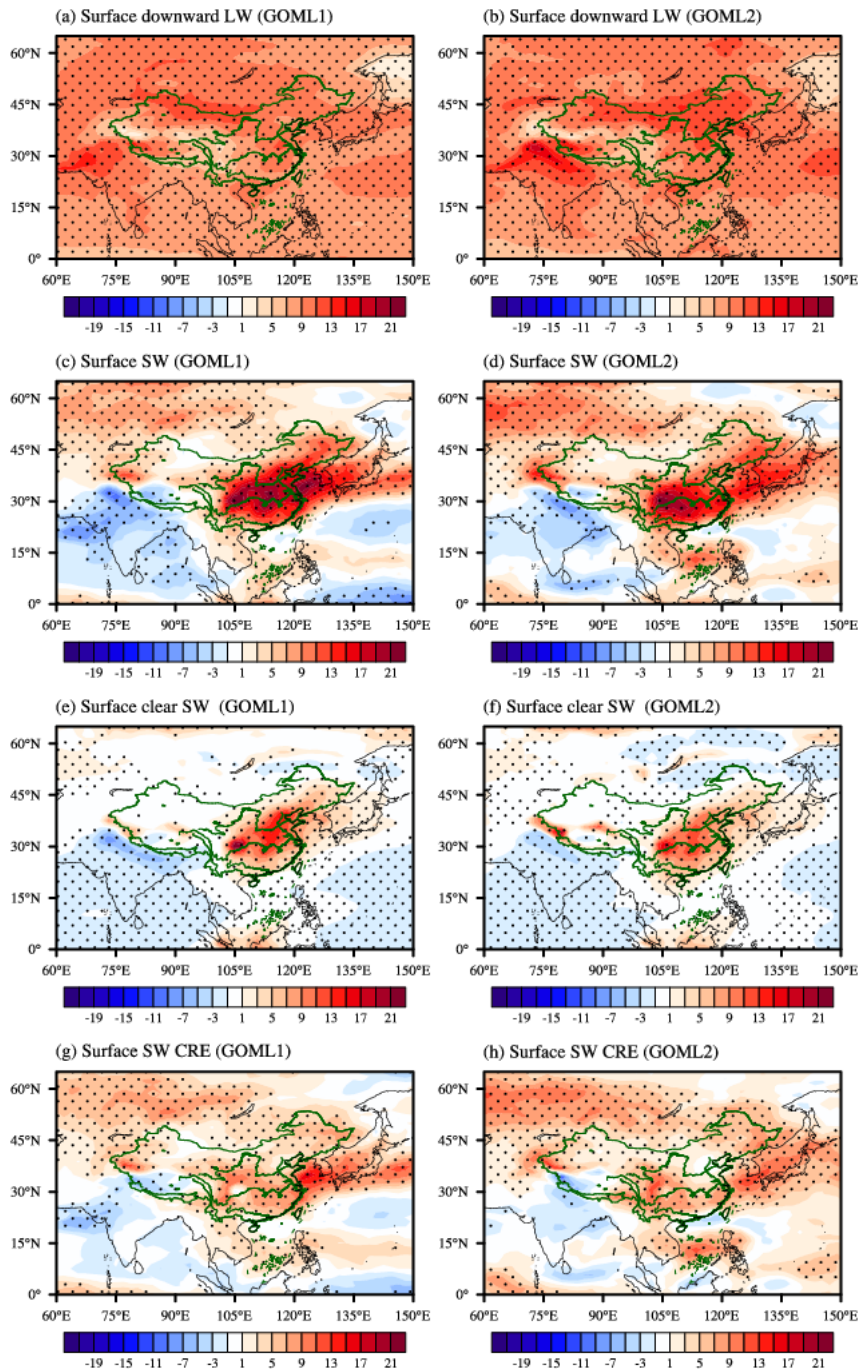
866

867

868

**Figure 8.** Area averaged total, mean temperature change induced, temperature variability-change induced future changes in frequency (units: events/year; a and b), intensity (units: °C/day; c and d), and duration (units: days; e and f) of compound, daytime, and nighttime HWs over whole China in MetUM-GOML1 (left panels) and MetUM-GOML2 (right panels).





869

870 **Figure 9.** Spatial patterns of future extended-summer-mean changes in surface downward LW

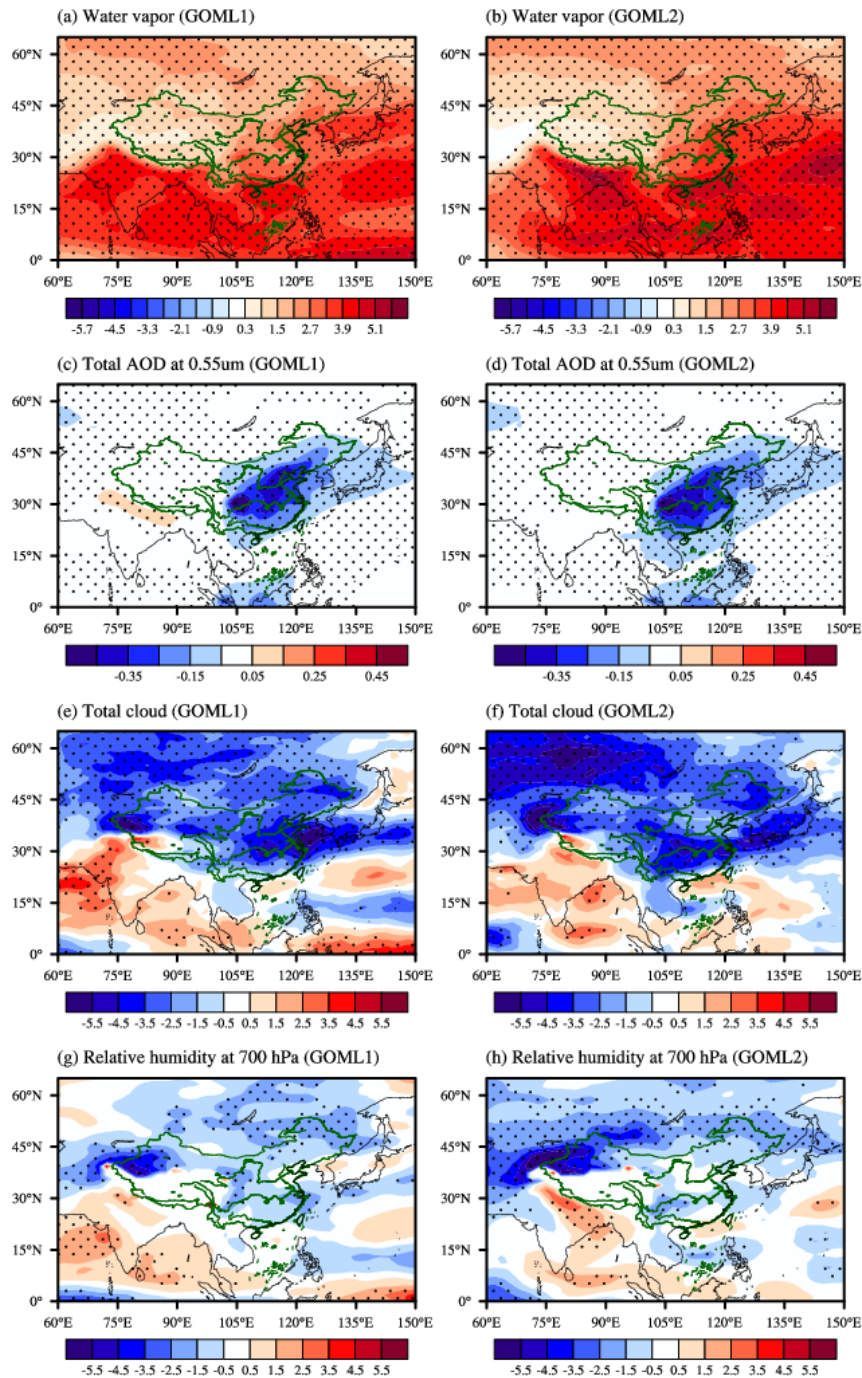
871 radiation (a and b), net surface SW radiation (c and d), surface clear SW radiation (e and f), and

872 surface SW CRE (g and h) in MetUM-GOML1 (left panels) and MetUM-GOML2 (right panels).

873 Radiation with positive value meaning downward and in  $W m^{-2}$ . The black dots highlight regions

874 where the changes are statistically significant at the 90% confidence level based on a two-tailed

875 Student's *t*-test.



877

878 **Figure 10.** Spatial patterns of future extended-summer-mean changes in column-integrated water879 vapor (a and b; units: kg m<sup>-2</sup>), total AOD at 0.55 um (c and d), total cloud cover (e and f; units: %),

880 and relative humidity at 700 hPa (g and h; units: %) in MetUM-GOML1 (left panels) and MetUM-

881 GOML2 (right panels). The black dots highlight regions where the changes are statistically

882 significant at the 90% confidence level based on a two-tailed Student's *t*-test.

